

Accepted to The Astrophysical Journal Supplement May 26, 1998

AN OPTICAL/NEAR-INFRARED STUDY OF RADIO-LOUD QUASAR ENVIRONMENTS I. METHODS AND $z=1-2$ OBSERVATIONS

Patrick B. Hall ^{1 2}

Steward Observatory, The University of Arizona, Tucson, Arizona 85721

Electronic Mail: hall@astro.utoronto.ca

Richard F. Green

National Optical Astronomy Observatories, Tucson, Arizona 85726-6732

Electronic Mail: rgreen@noao.edu

Martin Cohen

Radio Astronomy Laboratory, 601 Campbell Hall, University of California, Berkeley, California 94720

and Vanguard Research, Inc., Suite 204, 5321 Scotts Valley Drive, Scotts Valley, California 95066

Electronic Mail: mcohen@astro.berkeley.edu

ABSTRACT

We have conducted an optical/near-infrared study of the environments of radio-loud quasars (RLQs) at redshifts $z=0.6-2.0$. In this paper we discuss the sample selection and observations for the $z=1.0-2.0$ subsample and the reduction and cataloguing techniques used. We discuss technical issues at some length, since few detailed descriptions of near-IR data reduction and multicolor object cataloguing are currently available in single literature references.

Our sample of 33 RLQs contains comparable numbers of flat- and steep-radio-spectrum sources and sources of various radio morphologies, and spans a similar range of M_{abs} and P_{rad} , allowing us to disentangle dependence of environment on optical or radio luminosity from redshift evolution.

We use the standard “shift-and-stare” method of creating deep mosaiced images where the exposure time (and thus the RMS noise) at each pixel is not constant across the mosaic. An unusual feature of our reduction procedure is the creation of images with constant RMS noise from such mosaics. We adopted this procedure to enable use

¹Visiting Student, Kitt Peak National Observatory, National Optical Astronomy Observatories, operated by AURA Inc., under contract with the National Science Foundation.

²Current address: Department of Astronomy, University of Toronto, 60 St. George Street, Toronto, Ontario, Canada M5S 3H8

of the FOCAS detection package over almost the entire mosaic instead of only in the area of deepest observation where the RMS noise is constant, thereby roughly doubling our areal coverage.

We correct the object counts in our fields for stellar contamination using the SKY model of Cohen (1995) and compare the galaxy counts to those in random fields. Even after accounting for possible systematic magnitude offsets, we find a significant excess of $K \gtrsim 19$ galaxies. Analysis and discussion of this excess population is presented by Hall & Green (1998).

Subject headings: Methods: Data Analysis — Surveys — Quasars: General — Stars: General — Galaxies: General, Clusters of Galaxies

1. Introduction

The study of high-redshift galaxies and clusters is interesting because the light we see from them was emitted when galaxies and clusters were billions of years younger, and likely very different, than they are today. Since deep field galaxy surveys have only begun to identify large numbers of $z > 1$ galaxies (Steidel *et al.* 1996), it is useful to seek other efficient methods to find galaxies and clusters at $z > 1$.

One such possible method is to look for galaxies associated with quasars, specifically radio-loud quasars (RLQs). Radio-quiet quasars (RQQs) are rarely found in clusters at any redshift, but $\sim 35\%$ of intrinsically luminous ($M_B < -25$) RLQs are located in clusters of Abell richness class 0–1 (and occasionally 2) at $z = 0.5$ – 0.7 (Yee & Green 1987). However, little work has previously been done on RLQ environments at $z > 0.7$.

Some RLQs show possible additional evidence for being located in rich environments, in the form of an excess number of “associated” C IV (Foltz *et al.* 1988) or Mg II (Aldcroft, Bechtold & Elvis 1994) absorption systems. (For our purposes we define “associated absorption” to mean C IV or Mg II systems located within ± 5000 km s⁻¹ of the quasar redshift.) These systems may arise in gas expelled at high velocity from the quasars or in galaxies in clusters at or near the quasar redshifts. In the last few years high-resolution Keck spectra have shown that some associated C IV systems are unlike the typical intervening C IV absorption systems. These “intrinsic” systems show unusually smooth and broad line profiles, or well-resolved optically thick but shallow lines indicating partial coverage of the background emission (Hamann, Barlow & Junkkarinen 1997; Hamann *et al.* 1997). Variability has also been seen in a few cases (Hamann *et al.* 1995; Hamann, Barlow & Junkkarinen 1997; Aldcroft, Bechtold & Foltz 1997). Associated C IV absorbers with these characteristics are almost certainly produced by gas associated with the quasar central engine. It is also possible that the excess associated Mg II absorbers of Aldcroft, Bechtold & Elvis (1994) are intrinsic to their low-luminosity steep-radio-spectrum sample, since it is the

only sample to date to show an excess of associated Mg II. However, as the number of quasars with associated absorption which have been studied in detail is small, it remains possible that a substantial fraction of such quasars reside in clusters which produce associated absorption.

In 1994 we embarked upon a project to extend studies of quasar environments beyond $z \sim 0.6$. The goals of this project are to study the environments of RLQs from $z = 0.6$ – 2.0 , to study the correlation, if any, between RLQ environment and other quasar properties such as the presence of associated absorption, and to study any examples of high-redshift galaxies and/or clusters found in high-redshift RLQ fields. To study galaxies at redshifts $z > 0.6$ requires deep imaging, preferably in the rest-frame optical and near-IR where galaxies emit most of their stellar light. Thus this project used K_s band (2.0 – $2.3 \mu\text{m}$) imaging to sample the rest-frame near-IR at the quasar redshifts, supplemented by Gunn r (0.6 – $0.7 \mu\text{m}$) imaging to sample the rest-frame near-UV. Early-type galaxies which formed at $z \gg 2$ will have very red colors in $r - K_s$ at $z > 1$, which helps to distinguish any clustering around the quasars from the field galaxy population.

This paper discusses our observations for a study of RLQ environments at $z = 1$ – 2 . A $z = 0.6$ – 1 sample will be presented in a future paper. In §2 we outline the selection of targets, in §3 we discuss the observations and the data reduction and analysis techniques used, and in §4 we compare the galaxy counts in our fields to those in random fields. In Paper 2 (Hall & Green 1998) we examine the properties of galaxies in $z = 1$ – 2 RLQ fields, present the evidence for an excess population of faint galaxies which are plausibly associated with the quasars, and discuss the properties of these candidate high-redshift galaxies and clusters.

2. Sample Selection

Our quasar sample was designed to cover the redshift range $z = 0.6$ – 2.0 fairly evenly, to contain comparable numbers of flat- and steep-radio-spectrum sources and sources of various radio morphologies, and to span a similar range of M_{abs} and P_{rad} , allowing us to study how environment correlates with such properties at a given redshift and thus disentangle such effects from redshift evolution. We preferentially selected objects with known high- z intervening absorption properties, giving even more preference to objects with few such absorbers, to reduce confusion about with which system any detected excess galaxies are associated.

The sample was split into three redshift ranges. The $z = 0.6$ – 1.0 subsample was intended to extend previous quasar environment studies (which reached $z \sim 0.6$ – 0.7) to the highest redshift feasible using the Steward 61" and 90" telescopes. Data and analysis for this subsample will be presented in a future paper. The $z = 1.4$ – 2.0 subsample was selected to feasibly allow investigation of intrinsic C IV absorption systems with the KPNO 4-m telescope. The $z = 1.0$ – 1.4 subsample was selected to link the low- and high-redshift samples to provide a view of quasar environments over the entire redshift range $z = 0.6$ – 2.0 . Figure 1 shows the redshift histogram of the $z > 1$ quasars.

2.1. Radio Properties

In order to study the dependence of environment on as many factors as possible, in each redshift subsample we desired to span a similar range of M_{abs} and P_{rad} and to have an even split between flat and steep radio spectrum sources and between objects of different radio morphologies. Radio properties are given in Table 1.

Steep radio spectrum sources were defined as having $\alpha_r \geq 0.5$, where $S_\nu \propto \nu^{-\alpha_r}$ (Wills & Browne 1986). Radio spectral indices were taken from Stickel (personal communication) or from the NASA/IPAC Extragalactic Database (NED).³ Radio flux densities S_ν at 5 GHz were also taken from NED, and were converted to the radio power (luminosity) at 5 GHz rest frequency using α_r and assuming isotropic emission. Figure 2 is a graph of P_{rad} vs. z for the $z > 1$ objects. The average P_{rad} is 27.41 ± 0.57 for the $z=1-1.4$ sample, and 27.56 ± 0.36 for the $z=1.4-2.0$ sample, so they are well matched. However, because radio emission is not always isotropic (e.g. in the case of beaming), and again because radio variability affected both the measured S_ν and α_r , our values of P_{rad} should be considered representative only.

2.2. Moderate Redshift Subsample ($1.0 < z < 1.4$)

In this subsample we tried to exclude quasars with known associated and/or intervening Mg II or C IV, although in practice not many objects in our sample in this redshift range have been surveyed for absorption of either kind. Candidate objects for this redshift range were RLQs from the Large Bright Quasar Survey (Hooper *et al.* 1995), 1 Jy RLQs (Stickel & Kühr 1996) with existing R images obtained by Stickel, and HST QSOALS Key Project targets (Kirhakos *et al.* 1994), supplemented with RLQs from Aldcroft, Bechtold & Elvis 1994, Steidel & Sargent 1992, York *et al.* 1991, Spinrad *et al.* 1985, Dunlop *et al.* 1989, and Junkkarinen, Hewitt & Burbidge 1991 (see also Junkkarinen, Hewitt & Burbidge 1992) which had little or no absorption along the line of sight. Due to poor weather, the final sample of observed $z=1.0-1.4$ quasars consists of only 12 objects: 5 flat-spectrum, 6 steep-spectrum, and 1 of unknown radio spectral slope. Basic information on the objects is given in Table 2, and radio properties in Table 1. Information on intervening and associated absorption systems seen in the quasars' spectra is given in Table 3. Three objects are known not to have associated absorption, and one is; the rest have no published associated absorption information.

³The NASA/IPAC Extragalactic Database (NED) is operated by the Jet Propulsion Laboratory, California Institute of Technology, under contract to NASA.

2.3. High Redshift Subsample ($1.4 < z < 2.0$)

This subsample is further divided in two: the “absorbed” subsample of quasars with associated C IV absorption of rest-frame equivalent width (REW) $>1.5 \text{ \AA}$ within 5000 km s^{-1} of the quasar emission redshift z_e and the “unabsorbed” subsample of quasars without such absorption. We selected targets from the unpublished Radio-Loud Survey of Foltz *et al.*, targets with $z_a > z_e$ absorption as listed by Junkkarinen 1988, and targets from Foltz *et al.* 1986 and Barthel, Tytler & Thomson 1990. Targets were prioritized based on lack of high-redshift intervening absorption and having M_{abs} and P_{rad} in a range comparable to targets in the unabsorbed subsample.

The unabsorbed subsample contains quasars at $z=1.4\text{--}2.0$ with no C IV absorption of any strength within 5000 km s^{-1} of z_e . Quasars with known associated Mg II absorption were also excluded as a precaution. Targets were selected from the catalogs of York *et al.* 1991, Junkkarinen, Hewitt & Burbidge 1991, Barthel, Tytler & Thomson 1990, and Steidel & Sargent 1992, based on the same criteria as the absorbed subsample. The presence of intervening Mg II absorption systems was considered less problematic than C IV because the work of Steidel, Dickinson & Persson (1994) shows that intervening Mg II absorbers can be statistically identified and excluded from the analysis, even at these high redshifts.

The final sample of observed $z=1.4\text{--}2.0$ quasars is given in Table 2 and consists of 21 quasars: 8 flat-spectrum and 13 steep-spectrum; 14 with and 7 without associated C IV absorption. Basic information on the objects is given in Table 2 and radio properties in Table 1. Table 2 also lists the coordinates of two control fields intended for use with the $z>1$ quasar fields. Information on intervening and associated absorption seen in the quasars’ spectra is given in Table 3.

3. Observations, Data Reduction, and Object Cataloging

Optical observations were made in the Gunn r , i , and z bands, with a handful of observations in Kron-Cousins R_C , R' (see §3.4), and Mould I , which is very similar to Kron-Cousins I_C and is calibrated to it. Near-infrared (used here to mean wavelengths from $1\text{--}2.5 \text{ \mu m}$) observations were made in KPNO J , IRTF H , and 2MASS K_s (McLeod *et al.* 1995) bands, with a handful of observations in the Steward J and K bands. Figure 3 shows the throughput of all filters after accounting for the CCD or infrared array quantum efficiency.

3.1. Near-Infrared Observations

Observations of $z>1$ targets and two moderately deep control fields were made in the K_s and J filters using the Kitt Peak National Observatory 4-meter Mayall telescope and Infra-Red Imager (IRIM), a 256×256 NICMOS3 HgCdTe array with gain of $10.46 \text{ e}^-/\text{ADU}$ and read noise of 35 e^- (Probst 1995). The pixel scale was $0''.603$ at K_s and $0''.608$ at J . There is a slight pincushion

distortion in the IRIM field of view (Steidel, personal communication) for which no correction was made.

Images were typically taken in 4×4 raster patterns with $15''$ steps, $<10''$ offsets between patterns, and 1 minute integrations per position. Faint UKIRT standards (Casali & Hawarden 1992) were used for photometric calibration. Minezaki *et al.* (1998a) found no color term between K and K_s for the UKIRT system, but see §4.1.

H -band images of Q 0835+580 and Q 1126+101 were obtained through service observations on IRTF made by B. Golisch on UT 970319 in clear conditions. NSFCAM was used with gain $10.0\text{ e}^-/\text{ADU}$, read noise 55 e^- , and pixel scale $0''.3$. Two 4×4 grids with $20''$ steps and 6 coadds of 10 seconds exposure at each position (32 minutes total) were made for each object.

3.2. Near-Infrared Data Reduction

To aid in the reduction of infrared array data, a collection of routines collectively entitled PHIRS (Pat Hall’s Infrared Imaging Reduction System) was developed to work within IRAF.⁴ PHIRS is available at the World Wide Web URL <http://iraf.noao.edu/iraf/web/contrib.html> or by contacting the first author. In general, “standard” data reduction techniques for infrared arrays were used (e.g. Cowie *et al.* 1990). The specific routines used are in some cases directly derived from those in the DIMSUM package (Stanford, Eisenhardt & Dickinson 1995) which is also available from the WWW URL given above.

3.2.1. Outline

A brief outline of the steps used to reduce infrared array data follows.

- 1) Nonlinearity correction (IRIM data only).
- 2) Dark subtraction.
- 3) First-pass flattening, using a “running skyflat” or domeflats.
- 4) First-pass sky subtraction, using a “running sky”.
- 5) Determination of image shifts and first-pass coadding.
- 6) Creation of individual-image object masks out of coadded image.
- 7) Second pass flattening (unless domeflats were used) and sky subtraction using object

⁴The Image Reduction and Analysis Facility (IRAF) is distributed by National Optical Astronomy Observatories, operated by the Association of Universities for Research in Astronomy, Inc., under contract to the National Science Foundation.

masking and photometric scaling.

8) Cosmic ray removal (optional).

9) Make and apply throughput correction to account for light reaching the detector without being focussed by the telescope (Steward 61" and 90" only).

10) Rotate and resample from different observing runs or telescopes to a common scale (if necessary).

11) Coadd second-pass (and possibly rotated) images with 2x2 pixel resampling.

12) Calculate appropriate scaling factors for nonphotometric data and re-coadd.

13) Remove low-level striping from coadded image, if necessary (IRIM only).

14) Photometric calibration.

Where necessary, the reduction steps are now discussed in detail.

3.2.2. *Nonlinearity Correction*

To correct for nonlinearity in the KPNO IRIM array at high signal levels, sequences of varying exposure time images of the illuminated flatfield screen was taken through a narrow $2.2\mu\text{m}$ filter during each run. A fit was made to the observed dark-subtracted signal versus the expected signal extrapolated from low light levels, accounting for the delay between biasing and the first (non-destructive) read of the array, when the array is accumulating charge which is not reflected in the final output value for each pixel. The fits were consistent between runs, so the results from all runs were combined to find a nonlinearity correction which was applied to all images.

3.2.3. *Flattening and Sky Subtraction*

The “running sky” method of flattening and/or sky-subtracting was first described by Cowie *et al.* (1990). Each image of the field, offset by a few arcseconds from the others, is first flattened using a median of the raw images taken immediately before and after it, and then sky-subtracted using a median of the flattened versions of the same images. (The order of these two operations can be reversed.) Typically 8 images total, 4 before and 4 after, were used (20 or 22 for NSFCAM).

Running sky-subtraction was used for all data, but domeflattening was used for IRIM and NSFCAM data. Using running skyflats alone or along with domeflats gave similar results of RMS noises $\sim 10\%$ higher than domeflats alone. This is probably because domeflats were typically constructed from a set of images with total signal $\sim 20\%$ higher than the skyflats.

3.2.4. Coadding Infrared Images

Extensive experimentation was done to determine the optimal parameters for coadding the data such that cosmic rays and other bad pixels were excluded, the photometry of both bright and faint objects was not significantly different from a simple average, and the RMS noise of the output image was as low as possible, to optimize the detection of faint objects. The weights used to make the final coadded image were the “optimal weights” of each image: the exposure time divided by the variance (the square of the image’s RMS noise, after iteratively rejecting cosmic rays and other outlying pixel values).

The low S/N of individual IR data frames and occasional bad pixels makes the interpolation required for fractional pixel shifting undesirable, but the large number of offset images taken of each field does make subpixel information recoverable. Thus each original pixel was typically replicated into four pixels (2×2) and the images coadded using integer shifts in units of these new pixels.

Our detection algorithm requires a constant RMS noise across the image (see §3.6). Thus along with each coadded image an exposure map was created, giving the total exposure time at each pixel. Assuming a constant sky background during the observations, at each pixel the coadded image will have RMS noise proportional to $(\text{exposure time})^{-1/2}$, i.e. higher at the edges of the image where the exposure time was less. By multiplying the square root of the exposure map image by the coadded image, the coadded image is normalized to constant RMS noise. However, when the sky background varies and the RMS noise does not scale as $(\text{exposure time})^{-1/2}$, a more elaborate method must be used to construct the normalization image; see §3.3.5.

3.2.5. Object Masking

When running flatfielding and/or sky-subtraction is used, small negative residuals in the final coadded image are present around the position of each such object, in the pattern of the dithering used to make the observations, because faint objects are not completely excluded when the median is determined. These residuals are eliminated by masking out objects detected in the first-pass coadd and making a second pass.

To make this object mask image, each first-pass coadded image was normalized to uniform pixel-to-pixel RMS using the square root of the exposure map. The normalized image was boxcar smoothed and pixels above ~ 5 times the smoothed-image RMS noise were flagged as objects, along with rings of width one pixel around these flagged pixels. Individual-image object masks were then copied from the coadded-image mask using the known offsets of each image. These masks were used in the second-pass flatfielding and sky-subtraction, and the second-pass images were used to make the final coadd.

3.2.6. Photometric Scaling

Since we wish to detect the faintest objects possible, we need to coadd many infrared images, possibly taken at very different airmasses. Thus it was decided to incorporate airmass corrections as multiplicative scalings to the individual images before coadding. Our K_s extinction coefficient was either 0^m027 or 0^m120 per airmass, (see §3.5.2), so corrections applied to different images typically differ by $<0^m05$ and always by $<0^m12$.

As is usual, our magnitudes and fluxes represent exoatmospheric values, i.e. values at zero airmass. It should be noted that the extinction coefficient derived from observations at airmasses >1 *underestimates* the extinction which occurs at airmasses <1 , i.e. in the upper atmosphere (Johnson 1965; Manduca & Bell 1979). This is due to the Forbes effect: light at wavelengths with large monochromatic extinction coefficients is removed at small (<1) airmasses, leaving primarily light at wavelengths with smaller monochromatic extinction coefficients at airmasses >1 . The Forbes effect is small in the optical but strong in the IR due to the many H₂O absorption lines. To avoid potential systematic errors, carefully designed photometric passbands should be used (Young, Milone & Stagg 1994).

Nonphotometric data were scaled to photometric data on the same field by identifying several relatively bright objects (excluding the quasars whenever possible) in the coadded image of all data on the field. Photometry was then performed on these objects in the individual images, discarding objects which fell on bad pixels. The relative scalings and weights for each image were then interactively examined and adjusted as necessary. Also, at this point, if necessary, data from different detector/telescope combinations with different zeropoints were multiplicatively scaled to a common zeropoint. This results in a higher weighting for data from more efficient detector/telescope combinations. The images were then re-coadded with these adjusted scalings and weights, yielding a coadded image calibrated to the photometric data in the field.

3.2.7. Destriping

On some 4-meter IRIM images, a pattern of “striping” is evident. This pattern is fixed on the sky but varies from field to field, so it is thought to be caused by scattered light from bright stars well out of the field of view (M. Dickinson, personal communication). Subtraction of smoothed versions of the object-masked images removed this pattern. Running this procedure on images which showed no striping showed that it did not introduce any systematic error in the photometry, but simply increased the photometric uncertainties by at most $\sim 5\%$.

3.2.8. Rotation

Instrument rotations relative to N-S on the sky are not exactly the same between runs and telescopes. Thus the images from each separate filter or observing run were first coadded independently, and these coadded images were used to determine the rotations between different observing runs or filters, as well as the relative pixel scale between different telescopes (see §3.2.9). Typically the rotation was $\lesssim 1$ degree, and the maximum observed value was ~ 3 degrees. One set of K_s images for each field was arbitrarily taken to have an angle of zero relative to true north, so the angle of the coordinate systems in these fields are expected to be good to only ± 1 degree RMS.

When images are rotated with linear interpolation, a gridlike pattern is evident on the final image, caused by the differing noise characteristics in regions where pixels are linear combinations of several original pixels. Rather than rotating the final coadd and having such a pattern present, cosmic-ray cleaned images were rotated with linear interpolation before coadding, despite the low S/N of the individual frames, so that the patterns on individual images were averaged over in producing the final coadd.

3.2.9. Resampling

All data in J and H was resampled to the K_s pixel scale. The final IR images have half the K_s pixel scale, or $0.3015''/\text{pixel}$, since they have been expanded 2x2 for better registration during coadding (§3.2.4). The resampling was done in the same step as the rotation, on the cosmic-ray cleaned images.

3.3. Optical Data Reduction

Observations in the Gunn r band were made for almost all $z > 1$ targets observed in the K_s band. A few fields were observed in the i , I , and z bands. Standard reduction procedures for CCD data were used. Additional tasks for interactively removing fringes and for coadding optical images in an accurate manner were developed to work within IRAF. A package containing these tasks, entitled PHAT (Pat Hall's Add-on Tasks), is available at the WWW URL <http://iraf.noao.edu/iraf/web/contrib.html> or by contacting the author.

The overall philosophy of the optical reductions is our desire for extracting realistic magnitudes and errors over the maximum area and depth possible from our imaging data. Extensive experimentation was done at all steps of the reduction process. One important point is that we found no method to reliably coadd images with substantial seeing variations and reject cosmic rays without rejecting valid pixels in the cores and/or wings of many objects and affecting photometry at the $\sim 5\%$ level. (McLeod (1994) also experienced this problem). Thus we removed cosmic rays before coadding.

3.3.1. *Outline*

A brief outline of the reduction steps for optical data follows.

- 1) Overscan subtraction.
- 2) Bias subtraction (and dark subtraction, if necessary).
- 3) Dome flattening.
- 4) Illumination correction using blank sky flats and/or twilight flats.
- 5) Removal of fringes and/or scattered light (if necessary).
- 6) Cosmic ray removal.
- 7) Reorient images from different observing runs, telescopes, or instruments to a common orientation, and rescale to a common gain (if necessary).
- 8) First-pass coadding of images, using photometric scaling.
- 9) Rotate and rescale images from different observing runs or telescopes to match the coordinate system of the infrared images.
- 10) Calculate appropriate scaling factors for nonphotometric data and re-coadd.
- 11) Photometric calibration.

Where necessary, the reduction steps are discussed in detail below.

3.3.2. *Illumination Correction*

Twilight flats were often used to improve the domeflattening. For the Steward 800x1200 CCD, and occasionally the 2kx2k CCD, it was necessary to also use sky flats from disregistered images taken at each position. Even then, some 800x1200 images showed gradients of up to 5%. The worst of these images were discarded, but in the interests of reaching the faintest magnitudes, images flat to only a few percent were sometimes used in producing the final coadds.

3.3.3. *Fringe and Scattered Light Removal*

Data taken in z and some i filters showed considerable fringing. Fringe images were created by medianing affected frames together and subtracting a heavily smoothed background. The fringe image was then scaled and subtracted from the affected images, using an iterative procedure until satisfactory results were obtained. Bright scattered light was sometimes subtracted from individual object-masked images using a similar procedure. Other, fainter scattered light was

masked out using the very useful IRAF task XRAY.XIMAGES.PLCREATE.

3.3.4. *Photometric Scaling*

As with the infrared images, we chose to remove extinction by scaling the individual images to a common airmass rather than determining a mean airmass for the final coadded image. See §3.5 for a discussion of the photometric calibration and determination of the extinction coefficients.

3.3.5. *Coadding Optical Images*

Unlike the near-IR images, where the FWHM of stellar images was 2–3 pixels (at a pixel scale of $0.6''$ /pixel or larger), in the optical images ($0.3''$ /pixel) the FWHM was often 5 pixels or more. The optical images also were taken over longer time spans, almost always including data from different nights, resulting in greater seeing variations between images. No method could be found to reliably coadd images with substantial seeing variations and reject cosmic rays without rejecting valid pixels in the cores and/or wings of many objects and affecting photometry at the $\sim 5\%$ level (McLeod (1994) also experienced this problem). Such a method is possible when two or more images are taken at the same position, e.g. CRREJ in STSDAS⁵. In principle this task could be adopted to cope with dithered images, but for our optical images cosmic rays were always removed prior to coadding.

The best method we found for removing cosmic rays was a slightly modified version of the DIMSUM task XZAP (Stanford, Eisenhardt & Dickinson 1995). The procedure was to subtract off a median-smoothed version of the image, identify the peaks on the resultant image as cosmic rays, and replace them on the original image with the median of the surrounding pixels. Typically a first pass was made using an object mask and a second pass without object masking but with a more restrictive cosmic ray detection criterion. Visual inspection and editing was done to remove the few obvious cosmic rays which survived the automated removal. The optical images were then coadded with a simple averaging and minimal (or no) pixel rejection.

Another difference between coadding infrared and optical data arises from the variable sky level in the optical. The sky background is higher in the infrared, but its variability at K_s is usually not extreme. However, variable night sky emission lines are present in the i and z bands, and the presence of the moon or of thin cirrus can affect the sky brightness in the optical on a short timescale, a problem exacerbated by the fewer number of optical images available for coadding. Because the sky level (and thus the RMS) varies between individual images, the coadded-image RMS no longer scales with the exposure time at each pixel. Thus instead of multiplying by

⁵STSDAS is distributed by the Space Telescope Science Institute, which is operated by the Association of Universities for Research in Astronomy, Inc., for the National Aeronautics and Space Agency.

the square root of the exposure time to normalize the image, it is necessary to multiply by the inverse of the expected RMS for each pixel. This normalization map was constructed by creating individual normalization images with a constant pixel value equal to the measured image variance, and then coadding together these images using a weighted average and offsets identical to those used to make the coadded image.

3.4. Notes on Specific Optical Datasets

Optical observations of a few fields were obtained somewhat differently from most fields. Fifteen minutes’ r -band exposure on Q 1718+481 was obtained by B. Jannuzi on UT 950702 using the Palomar 4m and COSMIC instrument. The zeropoint was found using an observation of HZ 44 and should be accurate to ± 5 –10%. Three hours’ exposure on Q 1258+404 was obtained in the Mould I -band by J. Saucedo on UT 970322 and 970325 using the SO 90'' and 2kx2k CCD. Photometric calibration was made to Kron-Cousins I_C (actually Cape I ; see Sandage 1997) assuming a standard extinction coefficient of 0^m.061/airmass. Without photometric observations of this field in Gunn i , we have not been able to find a satisfactory transformation from I_C to i , so we have left the magnitudes as I_C . Images of Q 2230+114 were obtained in Kron-Cousins R_C by C. Liu on UT951222 and UT951225 using the SO 90'' and 800x1200 CCD. Conditions were nonphotometric, so this field cannot be used to study the galaxy r – K_s color distribution.

Control field positions were selected from the Deep Multicolor Survey (Hall *et al.* 1996) with the sole requirement of having a bright spectroscopically confirmed star at their centers. Images were taken not in r but in R' , a filter very similar to standard Kron-Cousins R_C (and calibrated to it) but with less of a red tail. We converted R_C magnitudes to r using

$$r = R_C + 0.322 \tag{1}$$

which was derived from both Frei & Gunn (1994) and Fukugita, Shimasaku & Ichikawa (1995).

3.5. Photometric Calibration

Since observations at both optical and near-IR wavelengths were typically made in only a single color, no color terms were used in the photometric solutions for each filter. The equation used to find the zeropoint and extinction coefficients from standard star observations was the same for all filters:

$$m = M - c_0 + c_1 \times X \tag{2}$$

where m and M are the observed (instrumental) and true (calibrated) standard star magnitudes respectively, with $m = -2.5 \times \log_{10}(I)$ where I is the ADU/sec measured for the standard, c_0 is the zeropoint magnitude for 1 ADU/sec (note that we use a different sign than is conventional), c_1 is the extinction coefficient, and X is the airmass of the observation.

We express the zeropoint as a positive number so that each coadded image i with total exposure time T_{exp} has a zeropoint c_i written as:

$$c_i = c_0 + 2.5 \times \log_{10}(T_{exp}) \quad (3)$$

The zeropoint c_i is thus the magnitude of 1 ADU on the coadded image. Thus the magnitude of an object on coadded image i can be calculated as:

$$m_{obj} = c_i - 2.5 \times \log_{10}(counts) \quad (4)$$

where the object's counts are measured in ADU. For fields with CCD images with different gains, images were multiplied by their gains before coadding. The coadded image zeropoint was then adjusted by $+2.5 \times \log_{10}(gain)$ so that the calibration was appropriate for the new gain=1 images.

3.5.1. Steward 90" + CCD

Gunn r (Thuan & Gunn 1976), i (Wade *et al.* 1979), and z band (Schneider, Gunn & Hoessel 1983) observations with the Steward 800x1200 and 2kx2k CCDs on the 90" were calibrated using standards from Thuan & Gunn (1976), Wade *et al.* (1979), Kent (1985), Jørgensen (1994), and Schneider (1995, personal communication). For each observing run which was possibly photometric and had an adequate number of standards, the photometric zeropoint and extinction coefficient in each filter used were determined. When conditions were nonphotometric or sufficient data to determine the extinction coefficients reliably were unavailable an r -band extinction coefficient of 0.086 magnitude/airmass was assumed (Kent 1985). The formal uncertainties on our magnitudes are 0^m050 for r , 0^m034 for i , and 0^m038 for z . The RMS scatters in each filter's photometric solution agree well with the formal uncertainties.

3.5.2. KPNO 4-meter + IRIM

For J and K_s observations with IRIM on the KPNO 4-meter, photometric calibration was performed using UKIRT faint IR standards (Casali & Hawarden 1992). Data from all nights in each run were combined to solve for the photometric zeropoint and extinction coefficient in each band separately using the IRAF package PHOTCAL.

The February 1996 4-meter run had variable and often nonphotometric conditions. It was the only 4-meter run where J data was taken, so the uncertainties in the J calibration are slightly larger than for K_s or H . The formal 1σ uncertainty on our J magnitudes is $\pm 0^m063$. For K_s , the limited calibration data available for the February 1996 run were consistent with the December 1994 run, and so the latter calibration was used for both runs.

The K_s zeropoint was found to be $0^m071 \pm 0^m055$ brighter during the July 1995 run than the December 1994 run, possibly due to dust accumulation on the mirror. The extinction coefficients

were also found to be different between the December 1994 and July 1995 runs. Higher extinction in the summer is consistent with the findings of Krisciunas *et al.* (1987) for Mauna Kea and the predictions of Manduca & Bell (1979). Both values of the extinction are plausible: Stanford, Eisenhardt & Dickinson (1995) give 0^m09 /airmass for K observations at KPNO, equal to the average measured K extinction coefficient for KPNO quoted in Manduca & Bell (1979), whose calculations give 0^m053 and 0^m066 /airmass for K at KPNO during typical winter and summer conditions. The formal uncertainties on our K_s magnitudes are $\pm 0^m037$ for 1994 and $\pm 0^m054$ for 1995, but the RMS scatter between the two photometric solutions is $\pm 0^m118$.

No objects were observed in both runs to allow a direct check on the K_s photometry, so must consider what systematic error might have been introduced into our calibrated magnitudes if one or both photometric solutions are in error. In other words, our standard star observations indicated a difference in both the telescope+instrument combination (zeropoint) and atmosphere (extinction coefficient) between our 1994 and 1995 4m observing runs. However, in the extreme cases where the telescope+instrument, atmosphere, or both were in fact exactly the same during the 1995 run as the 1994 run and the difference in the photometric solutions is due to random error, we have introduced systematic offsets (and RMS uncertainties) of $K_s(1994-1995)$ of 0.071 ± 0^m055 , 0.140 ± 0^m099 , or 0.211 ± 0^m149 , respectively.

We stress that it is the zeropoint *plus* appropriate extinction uncertainties which determine the uncertainties in the calibrated magnitude system, rather than just the zeropoint uncertainties commonly quoted in the literature. For a further discussion of possible systematic errors in our data, see §4.2.

3.5.3. IRTF + NSFCAM

For the IRTF observations, three calibration observations of UKIRT standard #19 were made, all at airmass 1.2-1.22. The zeropoint was found to be 22.034 ± 0.057 , in excellent agreement with the NSFCAM manual value of -22.06 (Leggett & Deanult 1996). The data were corrected using the H -band extinction of 0.051 magnitudes/airmass observed for Mauna Kea by Krisciunas *et al.* (1987). The formal uncertainty on our H magnitudes is 0^m060 .

3.6. Object Detection, Classification, and Photometry

Prior to running object detection software on the final coadded images, several important steps must be taken to ensure easy production and calibration of accurate output catalogs.

3.6.1. Normalizing and Trimming the Coadded Images

First, the photometrically calibrated final coadded images of each field in each filter are normalized to uniform RMS pixel-to-pixel noise using the exposure or normalization maps, as appropriate (see §3.2.4 and §3.3.5). The images have already been rotated and resampled onto the same coordinate system (see §3.2.8, §3.2.9 and §3.3.1); they are now shifted to a common origin. The images are then masked so that only areas with a certain minimum exposure time (typically 0.25 times the maximum exposure time in the coadded image) are included in the trimmed image. Pixels outside such regions are set to zero. For fields with images in multiple filters, the images are masked to exclude pixels where any image has been set to zero.

For these trimmed images with uniform RMS, the detection significance of objects is constant across the image, i.e., a 3σ detection is a 3σ detection regardless of location on the image. However, the magnitude scale and thus the limiting magnitude is not constant across the image: the magnitudes of objects near the image edges will be erroneously faint, since the edges have higher noise and have been multiplied by some factor <1 to achieve constant RMS. This complication is worth overcoming, as this procedure increases the useful area of our coadded images by about a factor of 2 compared to the standard procedure of using only the area with maximum exposure, because of the small sizes of the IR arrays and CCDs used. Glazebrook *et al.* (1994) and Bershadsky, Lowenthal & Koo employed similar techniques for object detection, although not for photometry. Another approach to the same problem is to modify object detection programs to handle spatially varying RMS noise, e.g. FOCAS (Adelberger & Steidel 1996) or SExtractor (Nonino *et al.* 1998).

Once a catalog of objects is generated, the true magnitudes are computed by taking the central pixel of each object, determining the factor by which that pixel was multiplied to make the normalized image, and correcting the object’s magnitude to account for this factor. A similar procedure is used to calculate the area of sky surveyed as a function of limiting magnitude.

3.6.2. Summing Images in Different Filters

We are interested in galaxies detected in even just a single filter and wish to study such galaxies’ properties consistently (i.e. within the same aperture) in all filters. In particular, we are interested in objects in the $z>1$ quasar fields detected only in the near-IR. Thus we created a summed $r+K_s$ image (or $r+J+K_s$ where good J data was available) in each field. To give each filter’s image equal weight at the faintest magnitudes, all the input images were normalized to the same RMS before summing.

It is possible that an object detected just at the detection limit in one filter could fall below the detection limit in the summed image, since the summing would effectively just be adding noise to such a galaxy. We used the FOCAS task CLEAN to replace the isophotal area of all catalogued objects in the individual filter images with random sky values, and then inspected the images

visually. Typically only one or two faint ($<5\sigma$) blue galaxy candidates were overlooked in each field. The candidates were often smaller than the minimum area or were classified as “noise,” and the number of such candidates was consistent with the number of noise spikes seen by displaying the negative side of the sky histogram.

We chose not to smooth the images to the same PSF before summing and determining isophotes for photometry, despite its attractiveness for matching isophotes in different filters and reducing noise to assist in faint object detection. Tests of smoothing using IRAF IMMATCH.PSFMATCH and FOCAS showed that there was a systematic shift in the magnitudes of objects after smoothing, such that the objects were apparently fainter in the smoothed image. The shift was magnitude-dependent: fainter objects had a larger magnitude offset. This is understandable since smoothing will reduce noise, and at the faintest levels objects are difficult to distinguish from noise. It might be possible to avoid this bias for e.g. $>5\sigma$ objects by using a smaller convolution kernel than the 15×15 pixel ($\sim 4.5''\times 4.5''$) box we used, or by simply matching the FWHM of different images instead of the complete PSF shape as we attempted.

3.6.3. Object Detection

Object detection, classification, and photometry was performed with FOCAS (Valdes 1982a; Valdes 1982b). We used the built-in smoothing filter and required all detected pixels (in the smoothed image) to be at least 2.5 times the iterative image RMS above sky. We required initial detections to have a minimum area of 21 pixels (1.9 arcsec^2), although during the splitting phase a reduced criterion of 10 pixels was used to better separate overlapping objects. These values are appropriate for our typical seeing conditions. For fields where the $2.5\sigma_{sky}$ limit resulted in too many spurious detections, we retroactively excluded objects less than $3\sigma_{sky}$ above sky. For a handful of fields with spurious pixel-to-pixel correlations from destripping of subpixel resampling and shifting, or with poor seeing, FOCAS was rerun with a larger minimum area. These detection criteria adjustments were carefully chosen to ensure that they eliminated no obviously real objects down to our 5σ detection limits, and a negligible number to our 3σ limits.

3.6.4. Object Classification and Star/Galaxy Separation

To isolate the galaxies in our fields from noise and stars as best as possible, we broke object classification down into several steps. We believe our approach is robust down to $K_s=16.5$ – 18.5 depending on the field. However, we can also correct statistically for the expected star counts fainter than these limits, as detailed in §3.7.

First, automatic FOCAS classification was done using a different PSF template for each field. Obvious classification errors (e.g. residual cosmic rays not classified as noise) were corrected interactively. Objects classified “noise” and “long” were then removed from the catalog, leaving

a catalog with objects classified as either unresolved (star or fuzzy star) or resolved (galaxy or diffuse).

However, star-galaxy separation is only accurate above a certain S/N. To discriminate stars from galaxies down to this limit we use the resolution parameter R of Bernstein *et al.* (1994), defined as $R = m_c - m_t$ where m_c is the FOCAS “core” magnitude, the highest flux found in any contiguous 3x3 pixel area, and m_t is the FOCAS total magnitude (see §3.6.5). Both values are measured in the summed image of each field and thus they do not represent real magnitudes in any one filter. We plot R vs. m_t from one field in Figure 5, with objects classified as stars by FOCAS shown as crosses and all other objects as points. Stars form a locus of small R at bright magnitudes which runs into the galaxy locus at some magnitude dependent on depth, seeing, and pixel scale. We classify as stars objects brighter than this magnitude which have an R value below an upper limit defined such that all objects in the bright star sequence are still classified as stellar. This region is marked with the solid lines.

Lastly, seven fields (noted in Table 4) had useful WFPC2 snapshots available from the *HST* archive. For these fields we changed the R parameter classifications where necessary to match classifications determined by eye from the *HST* data. Such changes should have negligible effects on star or galaxy counts.

3.6.5. Object Photometry

The isophotes from the summed-image FOCAS catalog for each field were used to create catalogs for each individual filter, so that each object is measured within the same area in all filters. FOCAS total magnitudes (see next paragraph) are not expected to be affected by the small differences between PSFs in the summed and individual images; We have verified this by running FOCAS directly on the individual images. Images not used to make the summed image typically had worse seeing than those which were. Nonetheless, we still used the summed-image FOCAS total magnitude isophotes for these images. The same tests as above showed scatter consistent with photometric errors alone and no systematic errors in these cases as well, except for the *J*-band observations of Q 2345+061 (2''.68 seeing).

For our magnitudes we used FOCAS total magnitudes, which have been shown to be unbiased estimates of the true magnitudes of unresolved and Gaussian-profile objects (Koo, Ellis & Windhorst 1989; Bernstein *et al.* 1994; McLeod 1994; Neuschaefer & Windhorst 1995; but see Saracco *et al.* 1997). FOCAS total magnitudes are derived by growing each object’s original detection isophote until it doubles in size and then measuring the flux above the local sky in this aperture.

We make a minor correction to the FOCAS total magnitudes for split objects, whose total magnitudes are derived by apportioning the original object’s total counts among the split objects according to their isophotal areas. This does not take surface brightnesses into account. A bright

star and a low surface brightness galaxy with equal isophotal areas will have erroneous magnitudes (too low and too high, respectively) if they were originally detected as one object and later split by FOCAS. Also, the detection isophote can be rather bright for objects very close together which were barely split by FOCAS, leaving considerable flux outside it to be apportioned with the same problems as above.

To better estimate the total magnitudes of split objects, we examine the difference between their total and isophotal magnitudes on the summed image, m_t and m_i . As seen in Figure 4, objects which were never split have low values of $(m_i - m_t)/\sigma_t$ where σ_t is the uncertainty of the total magnitude m_t (see next paragraph). However, at bright magnitudes the uncertainties from photon statistics are quite small, and so this quantity is sensitive to erroneous estimates of m_t . Thus we empirically identified objects with $(m_i - m_t)/\sigma_t > 10$ and $(m_i - m_t) > 0^m3$ as objects whose m_t values are affected by splitting. For these objects we replaced the total counts c_t with $c_t = c_i + 1.5 \times \Sigma_t$, where c_i is the isophotal counts (in ADU) and Σ_t is the uncertainty of the FOCAS total magnitude, in ADU (see next paragraph). As seen in Figure 4, this approximates the average ‘‘aperture correction’’ of $\sim 1.5\sigma_t$ between c_t and c_i for objects which were never split more accurately than a fixed value would (compare Figure 4a and b).

We have also replaced the total counts with the isophotal counts in cases where the total counts were smaller, since the total magnitude should be brighter. We thank the referee for pointing out that such cases are expected since the total magnitude will have a larger uncertainty due to its larger aperture. Thus our correction has introduced a statistical bias to brighter magnitudes. However, only a small percentage of objects are affected (see Fig. 4a) and so the estimated effect of the bias is an erroneous brightwards shift in our magnitude bin centers of only 0^m01 – 0^m03 . This shift is not enough to significantly change any of our conclusions, so we have not recalculated all our magnitudes at this time. We plan to make our catalogs public in a future paper, and will correct this error at that time.

After these corrections to the FOCAS total counts were made, total magnitudes were calculated from them. FOCAS does not provide error estimates, so we calculated the error on the object counts Σ_t and the magnitude error σ_t as follows, assuming a constant RMS noise across the image:

$$\Sigma_t = (g \times c_t + (g \times \sigma_{sky})^2 \times A_t)^{1/2} \quad (5)$$

$$\sigma_t = 1.0857 \times \Sigma_t / (g \times c_t) \quad (6)$$

where g is the gain, A_t the area of the FOCAS total magnitude aperture, c_t the total counts within that aperture, and σ_{sky} the RMS noise of the image (the original image, for images which showed striping).

The average 3σ limiting magnitude was estimated for each filter from the magnitude-error graph before correction for RMS normalization (§3.6.1). Magnitudes fainter than this limit were set to the limiting value. The true normalization-corrected magnitudes were then computed by determining the factor by which the central pixel of the object was multiplied to make the

normalized image, and adjusting the object magnitude (or 3σ limit) appropriately. This assumes that the exposure time does not vary dramatically over the size of a typical object.

3.6.6. Galactic Extinction

We take the color excess $E(B-V)$ from Burstein & Heiles (1978, 1982) and R_λ from Mihalas & Binney (1981). We correct the limiting magnitudes and all objects’ magnitudes for Galactic extinction $A_\lambda=R_\lambda \times E(B-V)$ in each filter. Our adopted values of R_λ are given in Appendix A and the $E(B-V)$ values for each field in Table 4, along with the 3σ magnitude limits for each filter in each field.

3.6.7. Construction of Overall Catalogs

For each field, the individual filter catalogs were used to construct a catalog of objects with a $\geq 3\sigma$ detection within the FOCAS total magnitude aperture in either the r , K_s , or (when available) J filters. This is the faintest feasible catalog limit, since unresolved objects at the 3σ limit have only a $\sim 50\%$ chance of detection (Harris 1990). We use our “ 3σ catalog” to compare $N(m)$ counts with the literature. However, for reliable comparative studies of galaxy colors and counts between our different fields, this catalog was found to include too many spurious objects, since a spurious object in any filter becomes part of the catalog whereas most real objects are common to all catalogs. In addition, the errors on the colors become very large for objects below 5σ . Thus for most of our science we used a “ 5σ catalog,” consisting of all objects in the 3σ catalog brighter than the average 5σ K_s limit in each field. This catalog is essentially magnitude limited; but as long as the exposure time at the edges is $\geq 36\%$ of the maximum, the average 5σ K_s magnitude limit will be greater than the 3σ detection limit across the entire field.

We now consider several points of importance in understanding the reliability of our catalogs before making use of them scientifically.

(1) *Are our magnitudes and colors correct and on a system directly comparable to published data?* As mentioned in §3.6.5, FOCAS total magnitudes have been shown to be robust estimators of the true magnitudes of most types of faint galaxies, with the exception of large, low surface brightness objects near the detection limit. However, see §4 for a discussion of possible systematic errors in photometric calibration in our work and the literature.

(2) *How many spurious objects are contained in the catalogs?* We interactively removed obviously spurious objects in the halos and diffraction spikes of bright stars. Faint cosmic rays may make some objects spuriously bright, but the cosmic ray rate and our flux threshold for identifying them are both low enough that this should be a negligible effect. Misclassified stars will contaminate the galaxy catalog below our star-galaxy classification limit. The contamination

from stars is relatively small at faint magnitudes, but our fields are scattered over a wide range of Galactic latitude and longitude (see Table 2) and so stellar contamination cannot be ignored. We address the statistical subtraction of faint star counts from our fields in §3.7.

We make no correction for truly spurious objects in our 5σ catalogs. We reject objects classified as “noise” or “long” by FOCAS, and simulations (Neuschaefer, Windhorst & Dressler 1991) and observations by other researchers (Smail *et al.* 1995; Hogg *et al.* 1997) have shown that contamination by spurious objects in single-filter data is $\lesssim 5\%$ at the 3σ magnitude limit for the default FOCAS detection threshold, decreasing to essentially zero at the 5σ limiting magnitude. Thus we expect that essentially no $>5\sigma$ objects are spurious, and that at most $\lesssim 10\%$ of objects in our 3σ catalog with magnitudes fainter than the 5σ limit are spurious ($\lesssim 15\%$ for the four fields with J data).

(3) *How many real galaxies do we miss, as a function of magnitude?* Galaxies can be overlooked due to magnitude errors scattering them below our detection limits, due to crowding, and due to misclassification as noise or “long” objects by FOCAS or as bright stars by the R parameter. Misclassification is unlikely to exclude a significant number of galaxies (see §3.6.2). Thus by the *completeness* of our galaxy catalogs we refer to only the effects of crowding and magnitude errors.

The most sophisticated way to calculate the completeness is to calculate the completeness matrix \mathbf{C}_{ij} (Stetson 1990b; Moustakas *et al.* 1997; Hogg *et al.* 1997), which gives the probabilities P_{ij} that a galaxy of true magnitude m_i is detected with magnitude m_j . While this is still possible with our image normalization procedure, it is rather complicated. We opt instead to calculate just the completeness as a function of magnitude $C(m)$, accounting for the variation in limiting magnitude across the image as follows.

At magnitudes well above our limiting magnitudes we assume that the completeness $C(m)$ is affected only by crowding:

$$C(m) = \frac{A_{tot} - A(< m)}{A_{tot}} \quad (7)$$

where $A(< m)$ is the area on the sky covered by objects with magnitudes brighter than m . This conservatively assumes that a simulated object added to the images would not be split by FOCAS if it overlapped an existing object. At fainter magnitudes where it is possible that objects have been missed due to noise fluctuations, we must account for the variation in limiting magnitude across the image. We assume that completeness is a function of signal-to-noise only, ignoring its dependence on surface brightness. In each filter, we calculate the fraction f of simulated objects recovered by FOCAS as a function of counts in the normalized image, or equivalently as a function of $m_{norm} = z.p. - 2.5 \times \log_{10}(\text{counts})$, the magnitude measured on the normalized constant-RMS image. (The technical details of this procedure are given in the following paragraph.) We want to convert this to the recovery fraction $C(m_{real})$ as a function of m_{real} , the real magnitude of an object after the normalization correction. We know the area $A(\Delta m)$ of the image as a function of $\Delta m = m_{real} - m_{norm}$. Thus we calculate $C(m_{real})$ by summing over the fractional area at each Δm

multiplied by the fraction f of recovered simulated objects with a magnitude on the normalized image corresponding to that real magnitude:

$$C(m_{real}) = \sum_{\Delta m} \frac{A(\Delta m)}{A_{tot}} f(m_{real} - \Delta m) \quad (8)$$

We also accounted for galactic extinction A_λ in each filter of each field so that the final completeness values $C(m_{final})=C(m_{real} - A_\lambda)$ were for identical values of m_{final} in each field.

The exact procedure followed in adding simulated objects to the images of each field was as follows. We took the normalized images from all filters which went into the summed image. We used FOCAS CLEAN to remove from the normalized images objects with fewer total counts in the K_s filter than an object $\gtrsim 0^m5$ fainter than the 3σ limit in the summed image. (This step was of course repeated for brighter counts bins spaced every 0.5 in magnitude.) We then added unresolved objects 30 at a time to the cleaned images in each filter simultaneously, using the PSF of each image, a base color of $r - K_s=4$ and $J - K_s=1.5$ for the objects, and a random magnitude offset within the magnitude bin in each filter. (Thus the range of colors simulated is $\pm 0^m5$ around the base values.) We summed these altered images and reran FOCAS. Simulated objects should thus be recovered unless they merged with an object brighter than themselves in K_s and were not split by FOCAS. (Strictly speaking, this step should be repeated for each filter, each time removing objects fainter than the simulated objects *in that filter*.) This procedure yields the completeness in all filters simultaneously, albeit in different magnitude bins given by the average galaxy colors used. We repeated this procedure 34 times in each counts bin, each time including different randomly generated Poisson noise appropriate to the object’s counts and the image gain. We repeated the entire procedure for each field, taking into account its Galactic extinction. The results are shown in Figure 6, plotted against $m - m_{3\sigma}$ to enable direct comparison of fields of different limiting magnitudes. Unusually low completeness is typically due to poor seeing; unusually high completeness can be due to good seeing or to destriping (see §3.2.7). The 50% completeness magnitudes have a range of $\pm 0^m5$ around the average 3σ limiting magnitude, or equivalently the completeness at the 3σ limiting magnitude has a range of $\pm 30\%$.

We use these completeness fractions to correct our observed counts. Using point sources to determine completeness correction provides only a lower limit to the true counts of finite-sized galaxies (McLeod *et al.* 1995), and will bias the results near the detection limit. However, small average sizes are found for galaxies at the magnitudes we reach by deep ground-based imaging (Tyson 1988) and by *HST* (Im *et al.* 1995; Roche *et al.* 1997), so point sources will reasonably approximate the morphology of faint galaxies in the $\sim 1.5''$ seeing of our data.

3.7. Galaxy Number-Magnitude Relations and Statistical Stellar Contamination Corrections

An obvious first step in comparing our data to previous work is to compare the number of galaxies as a function of magnitude, but prior to that a correction for contamination by stars will be necessary.

Sources of uncertainty in number-magnitude counts include surface brightness threshold effects, confusion of multiple objects as a single object, splitting of a single object into several spurious components, incompleteness in the galaxy catalog, inclusion of spurious objects in the galaxy catalog, errors in the measured galaxy magnitudes, misclassification of stars as galaxies (and vice versa), field-to-field variations due to clustering, and Poisson noise due to the finite number of galaxies detected. As discussed in the previous section, the first three effects should be well accounted for by our completeness corrections, and the contribution of spurious objects should be small (Hogg *et al.* 1997). Magnitude errors are best accounted for by the completeness matrix which we have not calculated, but the simple $C(m)$ approach is acceptable. Poisson noise and field-to-field clustering variations are unavoidable but their expected strengths can be computed (see §3.7.1).

The misclassification of stars as galaxies at faint magnitudes can be corrected statistically if the observed stellar counts at bright magnitudes can be extrapolated to fainter magnitudes using a model of the Galaxy. The Bahcall & Soneira (1981) Galactic model for B and V has no published extensions to other wavelengths, although an estimate of the stellar luminosity function in K has been made using that model (Mamon & Soneira 1982). Building on the work of Wainscoat *et al.* (1992), Cohen (1993, 1994, 1995) has developed a Galactic model spanning wavelengths from 0.14–35 μm to which we have compared our K_s data. Cohen & Saracco (1998) and Minezaki *et al.* (1998b) apply the same model to their K_s field surveys (cf. Minezaki *et al.* 1998b). This model, dubbed SKY, includes contributions from the disk, bulge, halo, spiral arms, local spurs, Gould’s Belt, and molecular ring of the Galaxy.

We determined the K_s magnitude $K_{classlim}$ brighter than which stars were *robustly* separated from galaxies by plotting R vs. K_s for each field. (Blue stars can be identified to fainter than $K_{classlim}$ by using information in the r images, but at $K_s < K_{classlim}$ all stars should have been identified, regardless of color.) We binned in $0^m.5$ wide bins the counts of all objects in our fields, of stars only, and of galaxies only. The stellar $N(m)$ at $K_s < K_{classlim}$ matched the predictions from SKY to within the observational errors in all fields except Q 0736–063. The predictions were too high for this field, and we exclude it from the following analyses. To obtain the final $N(m)$ for each field, for each magnitude bin with $K_s < K_{classlim}$ we subtracted the observed stellar counts from the counts of all objects. For $K_s > K_{classlim}$ we conservatively subtracted the larger of the observed stellar counts in that bin or the counts as predicted by SKY. The 1σ errors for each magnitude bin were calculated using the number of all original objects in the bin, star or galaxy, and the tables of Gehrels (1986).

We consider briefly the Q 0736–063 field. The Galactic extinction $E(B-V)=0.27$ for this field is only an estimate, but this cannot explain the discrepancy. To bring the observed $N(m)$ in line with predictions would require our K_s magnitudes to be at least 0^m.5 too faint, or $E(B-V)\geq 1.85$. The $r-K_s$ vs. K_s diagram for this field is if anything biased toward a bluer color distribution than average, suggesting an overestimated rather than underestimated $E(B-V)$, and unequivocally rules out $E(B-V)\geq 1.85$. Thus in this field the predicted stellar $N(m)$ was scaled to the observed stellar $N(m)$ at $K_s < K_{classlim} = 16.5$ before subtraction from the the galaxy $N(m)$. The scaling factor was 0.545, or -0.263 in the log. The SKY counts are estimated to be uncertain by ~ 0.16 in the log (Minezaki *et al.* 1998b, Figure 2). The resulting galaxy counts are consistent with those of McLeod *et al.* (1995), but we do not consider this field in future analyses since its $E(B-V)$ is only an estimate.

Figure 7 shows the $N(m)$ relations for all our individual fields before and after correction for stellar contamination as detailed above. The striking feature of the graph is the large field-to-field scatter at a given magnitude. Post-correction fields are not plotted beyond the 50% completeness magnitude, explaining the apparently reduced scatter in those fields at $K_s > 19$. The stellar contamination correction, which noticeably reduces the counts at $K_s < 18.5$, only slightly reduces the field-to-field scatter. The field-to-field scatter spans a factor of ~ 0.4 in the log at $K_s = 20-21$; i.e. the highest measured surface density per bin is ~ 2.5 times the lowest. As shown in §3.7.1 below, this scatter is consistent with expectations for the angular clustering of faint K -selected galaxy samples, which is higher than for faint optically-selected galaxies.

To determine the average K_s $N(m)$ over multiple fields, the stellar contamination corrected galaxy counts in the desired fields were coadded at each magnitude, weighting by the area of each contributing field. We excluded the fields of Q 0736–063 (uncertain $E(B-V)$) and Q 1508–055 (shallow K_s and no r data), and magnitude bins with $< 50\%$ completeness. The average $N(m)$ for all 31 good RLQ fields with $|b| > 20^\circ$ (covering a total area of 221 arcmin²) is shown in Figure 8 (solid squares + solid line), along with counts from the literature (open or half-filled symbols). Our counts lie within the range found in the literature. At $16 \leq K_s \leq 19$, our $N(m)$ agrees quite well with the Hawaii surveys (Gardner, Cowie & Wainscoat 1993; Cowie *et al.* 1994) and the survey of McLeod *et al.* (1995). At $K_s \geq 19$, our results are higher than average and agree most closely with the counts of Soifer *et al.* (1994), which are as high or higher than any others in the literature, possibly due to their target fields being around known objects at high redshift. The excess is large enough that it cannot be explained by spurious objects fainter than the 5σ limit in each field even if they contaminate the catalog by 10% (0.04 dex) at those magnitudes (see §3.6.7).

3.7.1. Expected Faint Galaxy Clustering

As mentioned in §3.7, the field-to-field variation in galaxy counts is quite large. Poisson errors do not come close to explaining the observed variation. This result is expected, and is due to galaxy clustering.

We follow Djorgovski *et al.* (1995) in estimating the contribution of faint galaxy clustering to the field-to-field variation in our counts (see Glazebrook *et al.* 1994 for a more exact method). We assume an angular correlation function $w(\theta)=A_w\theta^{-0.8}$ (all θ measured in arcsec) and a simple circular top-hat window function of angular radius $\theta_0=(A/\pi)^{1/2}$, where A is the mean area of the fields in arcsec². The RMS variation due to clustering is then

$$1.2Nw(\theta_0)^{1/2} \tag{9}$$

where N is the mean number of galaxies per field. Carlberg *et al.* (1997) derive $w(\theta)=(1.31 \pm 0.15)\theta^{-0.8}$ for a sample of ≥ 250 objects with $K \leq 21.5$ and $K_{avg} \sim 19$ from the Hawaii surveys. We adopt this relation for our fields. Note that this clustering amplitude is about a factor of two higher than for optically selected galaxies in equivalent magnitude ranges. This is likely due to preferential selection of blue galaxies (which are less strongly clustered) at optical wavelengths.

The observed RMS field-to-field variation in our stellar-contamination-corrected quasar field galaxy counts agrees with the predictions of the Carlberg *et al.* $w(\theta)$ to within $\pm 25\%$ in various subsets of the data considered (magnitude limits from $K_s=19$ to 21, all fields, all 1994 or 1995 fields, all $z > 1.4$ or $z < 1.4$ fields). Figure 9 shows the counts in our individual fields along with points from the literature. At $K_s < 21$, individual field $N(m)$ values range from less than or equal to the lowest field survey values in the literature to above the highest.

4. Systematic Magnitude Scale Offsets

It is clear from Figure 8 that at $K_s \gtrsim 19$ our galaxy counts are higher than those of field surveys; i.e., there is an excess of galaxies in our combined RLQ fields. The larger excess at fainter magnitudes argues that the overall excess is not simply a random fluctuation in the counts, and in Paper 2 we will show that the excess does not have the same $r-K_s$ color distribution as the field population and that at least part of it is spatially concentrated around the quasars. However, the similarity of the slope of our fields' $N(m)$ counts and the literature counts is suggestive of a systematic offset in magnitude scales being responsible for at least some the difference in the counts. Before we can quantify the strength of the galaxy excess in these fields, we must consider the effects of systematic errors in our comparison of our $N(m)$ results with the literature.

4.1. Systematics Between Our Data and the Literature

Three “ K ” filters have been used for faint galaxy work: K , K' (Wainscoat & Cowie 1992), and K_s (McLeod *et al.* 1995). These are different passbands by definition, but the effective passbands can also be significantly altered by differences between filter sets at different observatories (see Bessell & Brett 1988) and by the atmospheric transmission at the telescope site. Fortunately,

most faint galaxy studies have been calibrated to one of two K -band photometric systems: the CIT system (Frogel *et al.* 1978) to which the Elias *et al.* (1982) standards are calibrated, or the UKIRT system (Casali & Hawarden 1992). Casali & Hawarden give the transformations

$$K_{CIT} = K_{UKIRT} - 0.018(J - K)_{UKIRT} \quad (10)$$

$$(H - K)_{CIT} = 0.960(H - K)_{UKIRT} \quad (11)$$

Typical faint galaxies with $J-K=1.5$ should be 0^m03 fainter on the K_{UKIRT} scale than on the K_{CIT} scale.

Our photometric calibration is to the K_{UKIRT} scale, though we have retained the notation K_s since our observations were in that filter. Soifer *et al.* (1994), Minezaki *et al.* (1998a), and Dickinson *et al.* (1998) also observe in K_s and calibrate to K_{UKIRT} . Minezaki *et al.* find no color term between K_s and K_{UKIRT} , but from the different isophotal wavelengths of the filters they estimate:

$$K_s = K_{UKIRT} + 0.04(H - K)_{UKIRT} \quad (12)$$

Like Minezaki *et al.*, we do not make this correction, instead assuming $K_s=K_{UKIRT}$ for the UKIRT standards. If the above relation is correct, then our $K_s=K_{UKIRT}+0.02$, assuming a typical color of $H-K=0.5$. In other words, our K_s magnitude scale (and those of Soifer *et al.*, Minezaki *et al.*, and Dickinson *et al.*) may be 0^m02 fainter than the K_{UKIRT} scale to which we claim we are calibrated. However, that one of us (MC) calculates $K_s=K_{UKIRT}-0^m019\pm0^m013$ for $(H-K)_{UKIRT}=0$, so the average difference between K_s and K_{UKIRT} may be less than $+0^m02$ for faint galaxies. We will assume a $+0^m02$ difference to be conservative.

Of the K surveys to which we have compared our data, those of McLeod *et al.* (1995), EES97, and the Hawaii group (Gardner, Cowie & Wainscoat 1993; Cowie *et al.* 1994) are on the CIT system. The McLeod *et al.* data were obtained using a K_s filter, and so may require a color term in the transformation to the CIT system, although they did not detect one in their data. Combining equations 10 and 12 above, with the same assumed average colors, we estimate $K_s=K_{CIT}+0.05$. Most of the remaining surveys, namely Djorgovski *et al.* (1995), Glazebrook *et al.* (1994), Moustakas *et al.* (1997), Minezaki *et al.* (1998a), Soifer *et al.* (1994), and the HDF (Dickinson *et al.* 1998), are on the UKIRT system, with the caveat for the latter three discussed in the previous paragraph. Lastly, the ESO surveys (Saracco *et al.* 1997) are on the K' system as derived from observations of Elias standards and the relation

$$K' = K_{CIT} + (0.20 \pm 0.04)(H - K)_{CIT} \quad (13)$$

given by Wainscoat & Cowie (1992). Combining this with equation 10, we obtain

$$K' = K_{UKIRT} - 0.018(J - K)_{UKIRT} + (0.19 \pm 0.04)(H - K)_{UKIRT} \quad (14)$$

Assuming average $J-K=1.5$ and $H-K=0.5$ as above, the ESO magnitude scale can be put on the CIT system by subtracting $0^m10\pm0^m02$ and on the UKIRT system by subtracting $0^m07\pm0^m02$.

These average transformations between systems are accurate to only a few percent since faint galaxies will show a range of colors. The differences between systems are rarely larger than the $\sim 0^m05$ typical zeropoint uncertainty quoted for the various surveys, although the actual uncertainty in the correction to exoatmospheric magnitudes may be larger if extinction coefficient uncertainties are large. Even if the systematic magnitude scale offsets are not large, they may be enough to explain the difference between our quasar field counts and the literature control field counts.

To test the effects of systematics, we attempt to place all available data on the UKIRT K magnitude scale. (We choose the UKIRT scale because accurate flux zeropoints are available for it; see Appendix A). We adjust data from this work, Dickinson *et al.*, Soifer *et al.*, and Minezaki *et al.* brightwards by 0^m02 . We adjust the McLeod *et al.* data brightwards by 0^m02 , and the ESO data (Saracco *et al.* 1997) brightwards by 0^m07 . We adjust all other literature data on the CIT system (namely the Hawaii surveys) faintwards by 0^m03 . We then linearly interpolate the counts back to the original bin centers where necessary and find the area-weighted average of the $N(m)$ from the different surveys. Since the ESO (Saracco *et al.* 1997) and Minezaki *et al.* (1998a) surveys are each ~ 170 arcmin² in size, they are the dominant contributors to the literature control field counts at $17 < K < 19$.

In Figure 10 we plot $N(K_{UKIRT})$ for our data and for the area-weighted average of all published random-field imaging surveys which reach $K_{UKIRT} \geq 17$ (i.e. excluding Soifer *et al.* 1994, EES97, and Dickinson *et al.* 1998), including formal uncertainties on the magnitudes. Area-weighted RMS error bars are plotted for the literature data, but they probably underestimate the true RMS fluctuations at each magnitude between fields of size similar to ours (~ 8 arcmin²), since much of the area at $K \lesssim 19$ comes from large surveys which are treated as single fields when computing the RMS. We also plot data from our 1994 and 1995 KPNO 4m runs separately for comparison. Even with everything calibrated onto the same magnitude scale, there is a significant offset between our quasar-field data and the control-field data.

Even if our simple offsets have in fact brought all surveys’ magnitudes onto a common scale, it is probable that there are more systematics present in these various datasets than we have removed (cf. the discussion of aperture correction differences by Djorgovski *et al.* (1995) and the discussion of the true CIT and UKIRT magnitude scale offsets above). In particular, near the faint end of all surveys there may be nonlinear offsets which depend on how “total” magnitudes were estimated. However, the only control fields we have reason to prefer are our own, and they are too noisy to use by themselves. Thus our best option is to compare our data to the average of all available random-field data and to remove those systematics we believe we can estimate.

4.2. Systematics Within Our Data

From Figure 10 we see that in the range $K_{UKIRT}=17-19$ our 1994 and 1995 data agree well in slope, but not in normalization. Figure 11a shows a closeup of this magnitude range. The RMS errors on the control field data are large enough that essentially all our data are in agreement with the control field data in this magnitude range, but the 1995 data lies consistently above the other datasets. A systematic offset of our 1995 data brightwards of our 1994 data is consistent with the possible zeropoint and extinction coefficient systematics discussed in §3.5.2.

The conservative assumption would be that the offset between our 1994 and 1995 data and between those data and the literature is due to systematic errors. However, a complication in untangling systematic effects from real differences is that the 1994 data are composed almost exclusively of $z>1.4$ quasars, and the 1995 data of $z<1.4$ quasars. Based on the $K-z$ relation of powerful radio galaxies, a brightest cluster galaxy (BCG) might be expected to have $K_{UKIRT}\sim 17$ at $z=1$ and $K_{UKIRT}\sim 18$ at $z=1.4$. Thus it is plausible that the difference between our 1994 and 1995 datasets is real, caused by the appearance of cluster galaxies at brighter apparent magnitudes in the 1995 ($z<1.4$) dataset.

Since we cannot *a priori* discriminate between these two possibilities, we will quantify the galaxy excess for both of them. Our liberal assumption is that no further systematics exist once all surveys have been put on the UKIRT K magnitude scale as described in §4.1. Thus our *liberal* magnitudes are K_{UKIRT} magnitudes, which we estimate are equal to as K_s-0^m02 as discussed in §4.1, and whose $N(m)$ relation is shown in Figure 10. Our conservative assumption is that our 1994 and 1995 data should be matched to each other and to the control field data at $17<K_{UKIRT}<18$; i.e. that systematic errors are responsible for the offsets between our two datasets and the control fields. We offset our 1994 K_{UKIRT} magnitudes 0^m06 faintwards and our 1995 K_{UKIRT} magnitudes 0^m12 faintwards to form our *conservative* magnitudes. As seen in Figure 11b, with these offsets our 1994 data exactly match the control field data at $K_{UKIRT}=17.5-18$, our 1995 data match at $K_{UKIRT}=17-17.5$, and all three datasets lie within each others' 1σ (RMS) error bars at $K_{UKIRT}=17-18$. Our conservative magnitude scale $N(m)$ relation is shown in Figure 12.

We give our control field counts in Table 5 and the area-weighted average of the published literature counts in Table 6, both converted to the K_{UKIRT} system as detailed above.

5. Conclusions

We have presented optical and infrared data for a sample of 33 radio-loud quasars (RLQs) at $z=1-2$, discussed our data reduction procedures, and shown that the galaxy number counts in our fields lie above those of random-field surveys in the literature. Paper 2 (Hall & Green 1998) presents an analysis and discussion of the excess galaxy population in these fields.

An unusual feature of our data reduction procedure is the image normalization procedure

(§3.2.4) which allows useful results to be obtained from the edges of the fields which have less than the full exposure time. The complications introduced by this procedure were in the end worth enduring, since otherwise we would have had very little data at $\theta > 80''$ from the quasars. Data at such large angular distances was extremely useful for confirming the existence and extent of the large-scale excess galaxy population and for measuring the richnesses of the smaller-scale excesses seen in many fields (see Paper 2).

The complications faced in establishing the random-field K -band counts for comparison with our quasar-field data (§4.1) arose from two sources: first, the higher field-to-field variation in K -band counts compared to optical counts; and second, lack of a commonly used well-defined photometric system at JHK . Regarding the first point, it is worth investigating whether random-field J and H -band observations show substantially smaller field-to-field variations than K -band observations. Regarding the second point, we echo the call of Cohen *et al.* (1992) for the adoption of a truly standard system of IR passbands designed to minimize site-to-site differences due to atmospheric variations. One such system is described by Young, Milone & Stagg (1994). At the least, until such time as such a system is widely available, we encourage extragalactic JHK observers (including ourselves) to pay more attention to photometric calibration of their data than typically done in the past. It would also be useful to have standard star measurements in K_s as well as K , since there can be a few percent difference between magnitudes in the two filters. Such data should be forthcoming shortly from the DENIS (Fouque *et al.* 1997) and 2MASS (Skrutskie *et al.* 1997) surveys.

It is clear from Figure 8 that at $K_s \gtrsim 19$ there is an excess of galaxies in our combined RLQ fields. The reality of this excess is not in doubt, but its magnitude is (§4). K_s data from our 1995 KPNO 4m run lies consistently above the 1994 dataset and the control fields, and a systematic brightwards offset of our 1995 data is consistent with possible systematic uncertainties in the K_s zeropoint and extinction coefficient for that run (§3.5.2). Thus we will conduct much of our analysis in Paper 2 in parallel for two magnitude scales: conservative (UKIRT K magnitudes, but corrected for each dataset so that its bright-end $N(m)$ relation matches the literature control fields, i.e. assuming the offsets are purely systematic errors) and liberal (UKIRT K magnitudes, i.e. assuming no systematics exist beyond those between our natural K_s and UKIRT K magnitudes as described in §4.1). Future photometric snapshots of our fields in a K filter on a well-calibrated system would reduce the uncertainties on the surface density of the excess galaxy population in these fields.

This work was part of a Ph.D. thesis at the University of Arizona. PBH acknowledges support from an NSF Graduate Fellowship and from NASA. MC acknowledges the past support of AFRL through Dr. S. D. Price, for the development of the SKY model under contract F19628-92-C-0090 with Vanguard Research Inc., and thanks NASA-Ames for partial support through cooperative agreement NCC 2-142 with Berkeley. We thank M. Dickinson for providing DIMSUM; D. Minniti, E. Hooper, C. Liu, B. Golisch, J. Saucedo, and B. Jannuzi for obtaining some of the data used

herein; J. Barnes and F. Valdes for patient IRAF help; the referee for helpful comments; and Vic Hanson, Dennis Means, and the rest of the Steward Observatory telescope operations staff.

This research has made use of observations made at the Kitt Peak National Observatory, National Optical Astronomy Observatories, which is operated by the Association of Universities for Research in Astronomy, Inc., under contract to the National Science Foundation, and at the Infra-Red Telescope Facility, which is operated by the University of Hawaii under contract to the National Aeronautics and Space Administration; the NASA/IPAC Extragalactic Database (NED), operated by the Jet Propulsion Laboratory, California Institute of Technology, under contract to NASA; and data from operations made with the NASA/ESA Hubble Space Telescope, obtained from the data archive at the Space Telescope Science Institute, which is operated by the Association of Universities for Research in Astronomy, Inc., under NASA contract NAS 5-26555.

A. Photometric Systems and Parameters

In this appendix we tabulate data related to the filters and photometric systems used in this work. For our consideration of spectral energy distributions (Paper 2), for each filter we need to know $S_\nu(m=0)$, the equivalent monochromatic exoatmospheric flux density (usually given in Jy) at zero magnitude. It is also useful to know the offset ΔAB to the AB magnitude system, which by definition has $S_\nu(m=0)=3631$ Jy for all filters (Fukugita *et al.* 1996). Unlike the standard *UBVRI* photometric system, the Thuan-Gunn system calibration is based on BD+17°4708 (an F subdwarf) which is defined to have $m = 9.5$ in all filters in the system.

We take $S_\nu(m=0)$ and ΔAB for *riz* and $R_T I_C$ from Windhorst *et al.* (1991; W91), who did their $R_T I_C$ optical imaging at the Steward 90", and for $R_C I_T$ from Fukugita, Shimasaku & Ichikawa (1995; FSI95). The numerical values are given in Table A1. For comparison, we also tabulate AB offsets from Frei & Gunn (1994; FG94) and FSI95, and calculate $S_\nu(m=0)$ from Table 9 of FSI95, taking into account the different primary calibration stars for *riz* and *I*. Note that FSI95 refer to our filters as Thuan-Gunn *r*, PFUEI *iz*, and Cousins *RI*. The largest differences (up to 12.4%) are for I_C .

In this work we deal with near-IR magnitudes calibrated onto both the UKIRT and CIT scales. In Table A2 we reproduce the values of $S_\nu(m=0)$ and ΔAB for *JHK* in both systems from Table 12.2 of MacKenty *et al.* (1997). It is important to remember that it is not just the magnitude scales of the UKIRT and CIT systems which differ, but the filter passbands as well. Thus an object can have $K_{CIT}=K_{UKIRT}$ and still have different equivalent monochromatic exoatmospheric fluxes in the two systems because the effective wavelengths of the filters are different. See §4 for discussion of our conversion between *K* and K_s on the UKIRT system.

The most recent published calibration of Vega (Cohen *et al.* 1992) indicates that its *JHK* fluxes (in Jy) are not equal to the defined zero magnitude fluxes in either the CIT or UKIRT systems. However, since the standards that define the CIT system were calibrated assuming

$J=H=K=0$ (Frogel *et al.* 1978; Elias *et al.* 1982) and the UKIRT K zeropoint is defined as identical to the CIT system for A0 stars, it can be argued that revised calibrations of Vega should be propagated through to change the flux zeropoints of the CIT and UKIRT systems. Thus in Table A2 we reproduce from Tables 1 and 2 of Cohen *et al.* (1992) the isophotal wavelengths ($\lambda_{iso} = \int \lambda F_{vega}(\lambda) S(\lambda) d\lambda / \int F_{vega}(\lambda) S(\lambda) d\lambda$ where $S(\lambda)$ is the system sensitivity; Cohen *et al.* 1992) and the exoatmospheric monochromatic flux densities at those wavelengths for Vega as observed in the UKIRT system at Kitt Peak and Mauna Kea. We adopt the appropriate one of these $S_\nu(m=0)$ values to convert our UKIRT system magnitudes to exoatmospheric flux densities.

Lastly, we note that the differences in flux zeropoints between magnitude scales given in Tables A1 and A2, and between other values in the literature not listed here, are generally small ($\leq 5\%$, and at most 10–15% in a few extreme cases). However, they will introduce errors of this magnitude into SEDs constructed from broadband photometry, which will increase the uncertainties and the frequency of erroneous results when comparing observed and model SEDs. Other systematic errors are very possibly present in our data (e.g. extrapolation to airmass=0 and calibration to the UKIRT or CIT scales regardless of zeropoint), but the addition of another possible source of error is still undesirable.

Table A1. Optical Filter and Photometric System Parameters

Filter	$F_\nu(0^m)$, Jy, W91	ΔAB , W91	R_λ	$F_\nu(0^m)$ FSI95/CRL85	ΔAB	ΔAB , FG94	λ_{eff} (\AA)	$\Delta\lambda$ (\AA)
R_C, R'	2.0	3071	+0.182	+0.117	6588	1568
R_T	3105	+0.176	2.0	3006	+0.205	+0.055 ^a	6585	1373
r	4365	-0.194	2.19	4398	-0.208	-0.226	6677	916
i	4786	-0.294	1.60	4721	-0.285	-0.296	7973	1353
I_C	2377	+0.466	1.3	2446	+0.429	+0.342	8060	1542
I_T	1.3	2324	+0.484	+0.309 ^a	8668	1725
z	4831	-0.304	1.20	4821	-0.308	...	9133	984

^aHighly uncertain value.

Note. — FG94 is Frei & Gunn (1994); FSI95 is Fukugita, Shimasaku, & Ichikawa (1995); W91 is Windhorst *et al.* (1991). We have adopted $R_V=3$ (Mihalas & Binney 1981) and have renormalized the R_λ values for Gunn *riz* from $R_V=3.05$ (Schneider, Gunn & Hoessel 1983). R_λ values for other filters are taken from Mihalas & Binney (1981). Zero-magnitude fluxes and AB offsets from various sources are listed in columns 2-3 and 5-7. Filter effective wavelengths λ_{eff} and widths $\Delta\lambda$ are from FSI95.

Table A2. Infrared Filter and Photometric System Parameters

Filter	Vega@KP	$F_\nu(0^m)$, Jy Vega@MK	UKIRT	CIT	Adopted ΔAB	R_λ	λ_{iso} , μm KP MK		$\Delta\lambda$, μm
J	1636.6	1631.0	1600	1670	+0.865 ^a	0.77	1.212	1.215	0.26
H	1049.5	1049.7	1020	980	+1.347 ^a	0.50	1.654	1.654	0.29
K	653.2	655.0	657	620	+1.862 ^a	0.29	2.182	2.179	0.41
K_s	665 \pm 8	+1.843 ^a	0.29	2.160	...	0.28

^aAdopted AB offsets are for Mauna Kea for H and for Kitt Peak for all other filters.

Note. — Exoatmospheric zero-magnitude fluxes are listed in columns 2-3 for UKIRT system filters at Kitt Peak (KP) and Mauna Kea (MK) assuming Vega has $J=H=K=0$ (Cohen *et al.* 1992), and in columns 4-5 for the CIT and UKIRT systems (MacKenty *et al.* 1997). R_λ values for all filters are taken from Mihalas & Binney (1981). Columns 8-9 list isophotal wavelengths from Cohen *et al.* (1992). For IRIM K_s , all quantities listed were calculated by Cohen for this work.

REFERENCES

- Adelberger, K., and Steidel, C. C. 1996, personal communication
- Aldcroft, T., Bechtold, J., and Elvis, M. 1994, *ApJS*, 93, 1
- Aldcroft, T., Bechtold, J., and Foltz, C. B. 1997, to appear in “Proceedings of the Workshop on Mass Ejection from AGN,” eds. N. Arav, I. Shlosman, and R. Weymann
- Antonucci, R. R. J., and Ulvestad, J. S. 1985, *ApJ*, 294, 158
- Bahcall, J. N., and Soniera, R. M. 1981, *ApJS*, 47, 357
- Barthel, P. D., Miley, G. K., Schilizzi, R. T., and Lonsdale, C. J. 1988, *A&AS*, 73, 515
- Barthel, P. D., Tytler, D. R., and Thomson, B. 1990, *A&AS*, 82, 339
- Bernstein, G. M., Guhathakurta, P., Raychaudhury, S., Giovanelli, R., Haynes, M. P., Herter, T., and Vogt, N. P. 1994, *AJ*, 107, 1962
- Bershady, M. A., Lowenthal, J. D., and Koo, D. C. 1998, *ApJ*, in press (astro-ph/9804093)
- Bessell, M. S., and Brett, J. M. 1988, *PASP*, 100, 1134
- Bridle, A. H., Hough, D. H., Lonsdale, C. J., Burns, J. O., and Laing, R. A. 1994, *AJ*, 108, 766
- Browne, I. W. A., and Perley, R. A. 1986, *MNRAS*, 222, 149
- Burstein, D., and Heiles, C. 1978, *ApJ*, 225, 40
- Burstein, D., and Heiles, C. 1982, *AJ*, 87, 1165
- Carlberg, R. G., Cowie, L. L., Songaila, A., and Hu, E. M. 1997, *ApJ*, 484, 538
- Casali, M., and Hawarden, T. 1992, *JCMT-UKIRT Newsletter*, 4, 33
- Cohen, M., Walker, R. G., Barlow, M. J., and Deacon, J. R. 1992, *AJ*, 104, 1650
- Cohen, M. 1993, *AJ*, 105, 1860
- Cohen, M. 1994, *AJ*, 107, 582
- Cohen, M. 1995, *ApJ*, 444, 874
- Cohen, M., and Saracco, P. 1998, in preparation
- Cowie, L. L., Gardner, J. P., Lilly, S. J., and McLean, I. 1990, *ApJ*, 360, L1
- Cowie, L. L., Gardner, J. P., Hu, E. M., Songaila, A., Hodapp, K.-W., and Wainscoat, R. J. 1994, *ApJ*, 434, 114
- Dalcanton, J. J., Spergel, D. N., Gunn, J. E., Schmidt, M. A., and Schneider, D. P. 1997, *AJ*, 114, 635
- Dickinson *et al.* 1998, in preparation
- Djorgovski, S., Soifer, B. T., Pahre, M. A., Larkin, J. E., Smith, J. D., Neugebauer, G., Smail, I., Matthews, K., Hogg, D. W., Blandford, R. D., Cohen, J., Harrison, W., and Nelson, J. 1995, *ApJ*, 438, L13
- Driver, S. P., Phillips, S., Davies, J. I., Morgan, I., and Disney, M. J. 1994, *MNRAS*, 268, 393
- Dunlop, J., Peacock, J., Savage, A., Lilly, S., Heasley, J., and Simon, A. 1989, *MNRAS*, 238, 1171
- Elias, J. H., Frogel, J. A., Matthews, K., and Neugebauer, G. 1982, *AJ*, 87, 1029
- Ellingson, E., Green, R. F., and Yee, H. K. C. 1991, *ApJ*, 378, 475 (EGY91)
- Fukugita, M., Shimasaku, K., and Ichikawa, T. 1995, *PASP*, 107, 945
- Fukugita, M., Ichikawa, T., Gunn, J. E., Doi, M., Shimasaku, K., and Schneider, D. P. 1996, *AJ*, 111, 1748
- Foltz, C. B., Weymann, R. J., Peterson, B. M., Sun, L., Malkan, M. A., and Chaffee, F. 1986, *ApJ*, 307, 504
- Foltz, C. B., Chaffee, F., Weymann, R., and Anderson, S. 1988, in “Quasar Absorption Lines: Probing the Universe” (Cambridge: Cambridge), 53

- Foltz, C. B., Chaffee, F., Weymann, R., and Anderson, S. 1997, unpublished
- Fouque, P., Bertin, E., Dec, P. A., and Chevallier, L. 1997, in “The Impact of Large Scale Near-IR Sky Surveys,” eds. F. Garzón, N. Epchtein, A. Omont, B. Burton, and P. Persi (Kluwer: Dordrecht)
- Frogel, J. A., Persson, S. E., Aaronson, M., and Matthews, K. 1978, *ApJ*, 220, 75
- Frei, Z., and Gunn, J. E. 1994, *AJ*, 108, 1476
- Gardner, J. P., Cowie, L. L., and Wainscoat, R. J. 1993, *ApJ*, 415, L9
- Gardner, J. P. 1995a, *ApJS*, 98, 441
- Gardner, J. P. 1995b, *ApJ*, 452, 538
- Gehrels, N. 1986, *ApJ*, 303, 336
- Glazebrook, K., Peacock, J. A., Collins, C. A., and Miller, L. 1994, *MNRAS*, 266, 65
- Gullixson, C. A., Boeshaar, P. C., Tyson, J. A., and Seitzer, P. 1995, *ApJS*, 99, 281
- Hall, P. B., Osmer, P. S., Green, R. F., Porter, A. C., and Warren, S. J. 1996, *ApJS*, 104, 185
- Hall, P. B., and Green, R. F. 1998, *ApJ*, in press (Paper 2)
- Hamann, F., Barlow, T. A., and Junkkarinen, V. 1997, *ApJ*, 478, 87
- Hamann, F., Barlow, T. A., Beaver, E. A., Burbidge, E. M., Cohen, R. D., Junkkarinen, V., Lyons, R. 1995, *ApJ*, 443, 606
- Hamann, F., Barlow, T. A., Junkkarinen, V., and Burbidge, E. M. 1997, *ApJ*, 478, 80
- Harris, D. E. 1990, *PASP*, 102, 949
- Hewitt, A., and Burbidge, G. 1993, *ApJS*, 87, 451
- Hill, G., and Lilly, S. 1991, *ApJ*, 367, 1
- Hintzen, P., Ulvestad, J., and Owen, F. 1983, *AJ*, 88, 709
- Hogg, D. W., Pahre, M. A., McCarthy, J. K., Cohen, J. G., Blandford, R., Smail, I., and Soifer, B. T. 1997, *MNRAS*, 288, 404 (astro-ph/9702241)
- Hook, I. M., McMahan, R. G., Boyle, B. J., and Irwin, M. J. 1994, *MNRAS*, 268, 305
- Hooper, E. J., Impey, C. D., Foltz, C. B., and Hewett, P. C. 1995, *ApJ*, 445, 62
- Hutchings, J. B., Gower, A. C., Ryneveld, S., and Dewey, A. 1996, *AJ*, 111, 2167
- Hutchings, J. B., Price, R., and Gower, A. C. 1988, *ApJ*, 329, 122
- Im, M., Casertano, S., Griffiths, R. E., Ratnatunga, K. U., and Tyson, J. A. 1995, *ApJ*, 441, 494
- Johnson, H. L. 1965, *Communications of the Lunar and Planetary Lab*, 3, 67
- Jørgensen, I. 1994, *PASP*, 106, 967
- Junkkarinen, V. 1988, in “Quasar Absorption Lines: Probing the Universe: The Poster Sessions,” (Cambridge: Cambridge)
- Junkkarinen, V., Hewitt, A., and Burbidge, G. 1991, *ApJS*, 77, 203
- Junkkarinen, V., Hewitt, A., and Burbidge, G. 1992, *ApJS*, 81, 409
- Kellermann, K. I., Sramek, R. A., Schmidt, M., Green, R. F., and Shaffer, D. B. 1994, *AJ*, 108, 1163
- Kent, S. M. 1985, *PASP*, 97, 165
- Kirhakos, S., Sargent, W. L. W., Schneider, D. P., Bahcall, J. N., Jannuzi, B. T., Maoz, D., and Small, T. A. 1994, *PASP*, 106, 646
- Koo, D., Ellis, R., and Windhorst, R. A., in “First ESO/ST-ECF Data Analysis Workshop,” ed. P. Grosbol, F. Murtagh, and R. Warmels (ESO: Munich), 19

- Krisciunas, K., Sinton, W., Tholen, D., Tokunaga, A., Golisch, W., Griep, D., Kaminski, C., Impey, C., and Christian, C. 1987, *PASP*, 99, 887
- La Franca, F., Gregorini, L., Cristiani, S., De Ruiter, H., and Owen, F. 1994, *AJ*, 108, 1548
- Landolt, A. 1992, *AJ*, 104, 340
- Lawrence, C. R., Bennett, C. L., Hewitt, J. N., Langston, G. I., Klotz, S. E., Burke, B. F., and Turner, K. C. 1986, *ApJS*, 61, 105
- Leggett, S., and Denault, T. 1996, *NSFCAM 256x256 InSb Infrared Array Camera User's Guide*, NASA Infrared Telescope Facility
- Lonsdale, C. J., Barthel, P. D., and Miley, G. K. 1993, *ApJS*, 87, 63
- Machalski, J., and Condon, J. J. 1983, *AJ*, 88, 1591
- MacKenty, J. W., *et al.* 1997, *NICMOS Instrument Handbook*, Version 2.0, (Baltimore: STScI)
- Mamon, G. A., and Soneira, R. M. 1982, *ApJ*, 255, 181
- Manduca, A., and Bell, R. A. 1979, *PASP*, 91, 848
- McCarthy, P. J., van Breugel, W., and Kapahi, V. K. 1991, *ApJ*, 371, 478
- McLeod, B. A. 1994, Ph.D. Thesis, University of Arizona
- McLeod, B. A., Bernstein, G. M., Rieke, M. J., Tollestrup, E. V., and Fazio, G. G. 1995, *ApJS*, 96, 117
- Mihalas, D., and Binney, J. 1981, *Galactic Astronomy*, (New York: Freeman)
- Minezaki, T., Kobayashi, Y., Yoshii, Y., and Peterson, B. A. 1998, *ApJ*, 494, 111 ([astro-ph/9709202](#))
- Minezaki, T., Cohen, M., Kobayashi, Y., Yoshii, Y., and Peterson, B. A. 1998, *AJ*, 115, 229 ([astro-ph/9710221](#))
- Moustakas, L. A., Davis, M., Graham, J. R., Silk, J., Peterson, B., and Yoshii, Y. 1997, *ApJ*, 475, 445
- Murphy, D. W., Browne, I. W. A., and Perley, R. A. 1993, *MNRAS*, 264, 298
- Neff, S. G., Hutchings, J. B., and Gower, A. C. 1989, *AJ*, 97, 1291
- Neff, S. G., and Hutchings, J. B. 1990, *AJ*, 100, 1441
- Neuschaefer, L. W., Windhorst, R. A., and Dressler A. 1991, *ApJ*, 382, 32
- Neuschaefer, L. W., and Windhorst, R. A. 1995, *ApJS*, 96, 371
- Nilsson, K., Valtonen, M. J., Kotilainen, J., and Jaakkola, T. 1993, *ApJ*, 413, 453
- Nonino, M., *et al.* 1998, *A&A*, submitted ([astro-ph/9803336](#))
- Price, R., Gower, A. C., Hutchings, J. B., Talon, S., Duncan, D., and Ross, G. 1993, *ApJS*, 86, 365
- Probst, R. 1995, *IRIM manual*, Kitt Peak National Observatory
- Rector, T. A., Stocke, J. T., and Ellingson, E. 1995, *AJ*, 110, 1492
- Roche, N., Ratnatunga, K., Griffiths, R. E., and Im, M. 1997, *MNRAS*, 288, 200
- Sandage, A. 1997, *PASP*, 108, 1193
- Saracco, P., Iovino, A., Garilli, B., Maccagni, D., and Chincarini, G. 1997, *AJ*, 114, 887 ([astro-ph/9706055](#))
- Schneider, D. P., Gunn, J. E., and Hoessel, J. G. 1983, *ApJ*, 264, 337
- Skrutskie, M. F. *et al.* 1997, in “The Impact of Large Scale Near-IR Sky Surveys,” eds. F. Garzón, N. Epchtein, A. Omont, B. Burton, and P. Persi (Kluwer: Dordrecht)
- Smail, I., Hogg, D. W., Yan, L., and Cohen, J. G. 1995, *ApJ*, 449, L105
- Soifer, B. T., *et al.* 1994, *ApJ*, 420, L1
- Spinrad, H., Marr, J., Aguilar, L., and Djorgovski, S. 1985, *PASP*, 97, 932

- Sprayberry, D., Impey, C. D., Irwin, M. J., and Bothun, G. D. 1997, *ApJ*, 482, 104
- Stanford, S. A., Eisenhardt, P. R. M., and Dickinson M. 1995, *ApJ*, 450, 512
- Steidel, C. C., Dickinson, M., and Persson, S. E. 1994, *ApJ*, 437, L75
- Steidel, C. C., and Sargent, W. L. W. 1992, *ApJS*, 80, 1
- Steidel, C. C., Giavalisco, M., Pettini, M., Dickinson, M., and Adelberger, K. L. 1996, *ApJ*, 462, L17
- Stetson, P. B. 1990, *PASP*, 102, 932
- Stetson, P. B. 1990, in “The Formation and Evolution of Star Clusters,” ed. Janes, K. (ASP: San Francisco), 88
- Stickel, M., and Kühr, H. 1996, *A&AS*, 115, 11
- Swarup, G., Saikia, D. J., Beltrametti, M., Sinha, R. P., and Salter, C. J. 1986, *MNRAS*, 220, 1
- Thuan, T. X., and Gunn, J. E. 1976, *PASP*, 88, 543
- Tyson, J. A. 1988, *AJ*, 96, 1
- Valdes, F. 1982a, *FOCAS User’s Manual*, Kitt Peak National Observatory, Central Computer Services, Tucson AZ
- Valdes, F. 1982b, *The Resolution Classifier*, in “Instrumentation in Astronomy IV,” *SPIE Proceedings*, Vol. 331
- van Breugel, W., Miley, F., and Heckman, T. 1984, *AJ*, 89, 5
- Visnovsky, K. L., Impey, C. D., Foltz, C. B., Hewett, P. C., Weymann, R. J., and Morris, S. L. 1992, *ApJ*, 391, 560
- Wade, R. A., Hoessel, J. G., Elias, J. H., and Huchra, J. P. 1979, *PASP*, 91, 35
- Wainscoat, R. J., and Cowie, L. L. 1992, *AJ*103, 332
- Wainscoat, R. J., Cohen, M., Volk, K., Walker, H. J., and Schwartz, D. E. 1992, *ApJS*, 83, 111
- Wills, D. 1979, *ApJS*, 39, 291
- Wills, B. J., and Browne, I. W. A. 1986, *ApJ*, 302, 56
- Windhorst, R. A., Burstein, D., Mathis, D. F., Neuschaefer, L. W., Bertola, F., Buson, L. M., Koo, D. C., Matthews, K., Barthel, P. D., and Chambers, K. C. 1991, *ApJ*, 380, 362
- Yee, H. K. C., and Ellingson, E., 1993, *ApJ*, 411, 43 (YE93)
- Yee, H. K. C., and Green, R. F. 1987, *ApJ*, 319, 28 (YG87)
- York, D. G., Yanny, B., Crofts, A., Carilli, C., Garrison, E., and Matheson, L. 1991, *MNRAS*, 250, 24
- Yoshii, Y., and Peterson, B. A. 1995, *ApJ*, 444, 15
- Young, A. T., Milone, E. F., and Stagg, C. R. 1994, *A&AS*, 105, 259

Table 1. $1 < z < 2$ RLQ Sample: Radio Data

Name	α_r	α_r Refs	Radio Morph. Class	LAS (")	LLS (kpc)	LAS Refs	S_ν , Jy (5 GHz, obs.)	P_{rad} , W/Hz (5 GHz, rest)
$z < 1.4$ Subsample								
0003–003	0.84	Stickel	FR II	5.50	37.92	mvk91	1.400	27.72
0149+218	0.20	2.7/5.0	CL	4.50	32.65	mbp93	1.080	27.63
1328+254	0.59	Stickel	C	0.20	1.39	huo83	3.240	28.02
1430–0046	1.16	1.4/8.4 ^a	0.027 ^b	26.09 ^b
1437+624	0.78	1.4/5.0	C	<0.13	<0.91	vmh84	0.796	27.51
1508–055	0.30	Stickel	C	3.00	21.35	huo83	2.330	27.90
1606+106	–0.42	Stickel	CL	6.50	46.53	mbp93	1.700	27.54
1718+481	C/CE?	<15.00	<104.56	kel94	0.124	26.60 ^c
1739+522	–0.68	Stickel	C	1.00	7.31	nhg89	1.130	27.36
2144+092	–0.23	Stickel	CE	2.30	16.13	mbp93	1.010	27.30
2230+114	0.50	Stickel	T	2.40	16.55	nhg89	3.650	28.03
2325+293	0.97	1.4/5.0	T	50.40	345.62	huo83	0.428	27.22
$z > 1.4$ Subsample								
0017+154	1.20	2.7/5.0	T	14.00	105.84	bri94	0.500	28.17
0033+098	0.54	1.4/5.0	T	8.00	60.38	law86	0.330	27.63
0232–042	0.49	2.7/5.0	T	13.10	96.30	huo83	0.620	27.58
0256–005	0.26	2.7/5.0	C	<1.00	<7.56	laf94	0.230	27.38
0352+123	0.63	2.7/5.0	T	7.00	52.16	nhg89	0.270	27.39
0736–063	0.24	2.7/5.0	CL	1.40	10.56	nhg89	1.190	28.04
0808+289	0.69	1.4/5.0	T	34.00	256.41	bar88	0.053	26.89
0831+101	0.80	1.4/5.0	T	30.00	225.30	nhg89	0.074	27.00
0835+580	0.86	1.4/5.0	FR II	16.00	118.60	mvk91	0.688	27.84
0926+117	0.60	2.7/5.0	T	7.00	52.55	bar88	0.180	27.29
0952+179	0.39	2.7/5.0	C?	$\lesssim 2.00$	$\lesssim 14.75$	swa86	0.740	27.64
1018+348	0.01	1.4/5.0	T	19.00	139.20	mc83	0.469	27.25
1126+101	0.05	2.7/5.0	T	19.00	140.64	bar88	0.310	27.16
1218+339	0.90	1.4/5.0	FR II	10.00	74.05	mvk91	0.869	27.95
1221+113	0.71	1.4/5.0	T?	2.00	15.02	bar88	0.146	27.26
1258+404	1.14	1.4/5.0	FR II	23.00	171.90	mvk91	0.301	27.69
1416+067	0.96	Stickel	T	1.60	11.75	swa86	1.500	28.14
1556+335	0.33	1.4/5.0	C	<1.00	<7.47	swa86	0.870	27.80
2044–168	0.06	2.7/5.0	CL	12.00	90.61	nhg89	0.800	27.80
2149+212	0.60	2.7/5.0	T?	2.00	14.83	lbm93	0.360	27.46
2345+061	0.83	2.7/5.0	T?	1.10	8.16	lbm93	0.270	27.43

Note. — Radio spectral α_r is for $S_\nu \propto \nu^{-\alpha_r}$. References for α_r are Stickel (personal communication) or NED if two numbers are given; the numbers are the observed frequencies (in GHz) between which α_r was calculated. All α_r provided by Stickel were measured between 2.7 and 5 GHz, observed. We have made no attempt to correct for radio variability, and since much of the data was obtained at different epochs our values of α_r should be considered representative only. Radio morphological categories are primarily from Neff & Hutchings (1990): C = core only; CE = extended core; CL = core + lobe; and T = core + 2-sided lobe (triple). We also include FR II = 2 edge-brightened lobes, with or without a core (McCarthy, van Breugel & Kapahi 1991). There is some overlap between the FR II and T categories since different references do not always distinguish between them. LLS (Largest Linear Size) calculated for $h=0.75$, $q_0=0.1$. LAS (Largest Angular Size) reference codes given below.

^a8.4 GHz flux from Visnovsky *et al.* 1992.

^b S_ν and P_{rad} calculated from 8.4 GHz observations and 1.4/8.4 GHz spectral slope.

^c P_{rad} calculated assuming $\alpha_r=0.5$.

References. — au85: Antonucci & Ulvestad 1985; bar88: Barthel *et al.* 1988; bp86: Browne & Perley 1986; bri94: Bridle *et al.* 1994; hpg88: Hutchings, Price & Gower 1988; hu083: Hintzen, Ulvestad & Owen 1983; hut96: Hutchings *et al.* 1996; kel94: Kellermann *et al.* 1994; laf94: La Franca *et al.* 1994; law86: Lawrence *et al.* 1986; lbm93: Lonsdale, Barthel & Miley 1993; mbp93: Murphy, Browne & Perley 1993; mc83: Machalski & Condon 1983; mvk91: McCarthy, van Breugel & Kapahi 1991; nh90: Neff & Hutchings 1990; nhg89: Neff, Hutchings & Gower 1989; nil93: Nilsson *et al.* 1993; pri93: Price *et al.* 1993; rse95: Rector, Stocke & Ellingson 1995; swa86: Swarup *et al.* 1986; wb86: Wills & Browne 1986; wil79: Wills 1979; vmh84: van Breugel, Miley & Heckman 1984.

Table 2. $1 < z < 2$ RLQ Sample: Basic Data

Name (1950)	Alt. Name	RA (1950)	Dec (1950)	l	b	z	α_r	Ass. Abs.
$z < 1.4$ Subsample								
0003–003	3C2	00:03:48.8	–00:21:07	99.2803	–60.8592	1.037	S	?
0149+218	PKS	01:49:31.8	+21:52:21	141.0586	–38.6010	1.320	F	?
1328+254	3C287	13:28:15.9	+25:24:37	22.4665	+80.9884	1.055	S	N
1430–0046	LBQS	14:30:09.9	–00:46:04	347.9486	+52.7950	1.0229	S	?
1437+624	OQ663	14:37:32.0	+62:24:48	103.5246	+50.6938	1.090	S	N
1508–055	4C–05.64	15:08:14.9	–05:31:49	353.9090	+42.9358	1.191	F	N
1606+106	4C10.45	16:06:23.4	+10:37:00	23.0283	+40.7886	1.226	F	?
1718+481	PG	17:18:17.6	+48:07:11	74.3750	+34.8295	1.084	?	?
1739+522	4C51.37	17:39:29.0	+52:13:10	79.5635	+31.7482	1.379	F	?
2144+092	PKS	21:44:42.5	+09:15:51	65.7957	–32.2623	1.113	F	?
2230+114	4C11.69	22:30:07.8	+11:28:23	77.4379	–38.5824	1.037	S	Y
2325+293	4C29.68	23:25:42.2	+29:20:39	102.0649	–29.8561	1.015	S	?
$z > 1.4$ Subsample and Control Fields								
0017+154	3C9	00:17:49.8	+15:24:16	112.0466	–46.5332	2.012	S	N
0033+098	4C09.01	00:33:48.2	+09:51:29	116.8355	–52.5604	1.920	S	Y
0232–042	4C–04.06	02:32:36.6	–04:15:11	174.4627	–56.1557	1.438	F	Y
0256–005	PKS	02:56:55.1	–00:31:55	177.1898	–49.2283	1.995	F	Y
0352+123	4C12.17	03:52:59.2	+12:23:03	177.4171	–30.2463	1.608	S	Y
0736–063	PKS	07:36:30.2	–06:20:03	224.1712	+7.5168	1.901	F	Y
0808+289	B2	08:08:32.1	+28:54:02	193.4684	+29.1280	1.887	S	Y
0831+101	87GB	08:31:57.6	+10:08:17	215.6129	+27.4227	1.760	S	Y
0835+580	3C205	08:35:10.0	+58:04:52	159.2600	+36.8963	1.534	S	Y
0926+117	4C11.32	09:26:01.0	+11:47:32	220.7837	+40.0883	1.750	S	N
0952+179	PKS	09:52:11.8	+17:57:45	216.4550	+48.3636	1.472	F	N
1018+348	B2	10:18:24.1	+34:52:29	190.3893	+57.1220	1.404	F	Y
1126+101	PKS	11:26:38.7	+10:08:32	250.7199	+64.0478	1.516	F	Y
1218+339	3C270.1	12:18:03.9	+33:59:50	166.3079	+80.6390	1.520	S	Y
1221+113	MC2	12:21:47.4	+11:24:00	279.9186	+72.7723	1.755	S	N
1258+404	3C280.1	12:58:14.1	+40:25:15	115.2582	+76.8404	1.660	S	N
1416+067	3CR298	14:16:38.8	+06:42:21	352.1603	+60.6665	1.430	S	Y
1556+335	87GB	15:56:59.4	+33:31:47	53.5683	+49.3725	1.646	F	Y
2044–168	PKS	20:44:30.8	–16:50:09	29.9668	–32.9346	1.937	F	Y
2149+212	4C21.59	21:49:26.1	+21:16:07	76.5797	–24.7840	1.536	S	N
2345+061	4C06.76	23:45:58.4	+06:08:19	96.2347	–53.1630	1.540	S	N
CtrlFld1	...	00:59:09.3	–00:59:55	128.6937	–63.4866
CtrlFld3	...	00:59:39.7	–00:51:18	128.9466	–63.3321

Note. — “Name” is the quasar’s coordinate designation in epoch B1950. α_r refers to radio spectral slope, given as S (steep spectrum), F (flat spectrum), ? (unknown), or Q (radio-quiet quasar). See Table 1 for detailed radio properties. “Ass. Abs.” refers to the presence or absence of associated C IV and/or Mg II absorption in the quasars’ spectra; an ? indicates that no information is available. See Table 3 for detailed intervening and associated absorption information.

Table 3. $1 < z < 2$ RLQ Sample: Absorption Line Data

Name	z_{quasar}	z_{abs}	Ion	Redshift Search Interval	Ion	References	Ass. Abs.?
$z < 1.4$ Subsample							
0003–003	1.037			
0149+218	1.320			
1328+254	1.055	none		0.59-1.06	Mg II	abe94	
1430-0046	1.0229			
1437+624	1.090	0.8723	Mg II	0.63-1.09	Mg II	abe94	
1508–055	1.191	none		1.02-1.20	C IV	abe94	
				0.12-1.20	Mg II	abe94	
1606+106	1.226			
1718+481	1.084			
1739+522	1.379			
2144+092	1.113			
2230+114	1.037	~1.037	C IV	1.00-1.05	C IV	wil95	Y
				0.13-1.04	Mg II	abe94	
2325+293	1.015			
$z > 1.4$ Subsample							
0017+154	2.012	1.3636	Mg II, C IV	1.15-2.25	C IV	y91	
		1.6250	Mg II, C IV	0.2-0.85	Mg II	y91	
		1.8723	C IV	1.1-1.25	Mg II	y91	
		1.9382	C IV	1.48-1.67	Mg II	jhb91	
0033+098	1.92	1.7776	Mg II, C IV	1.46-1.95	C IV	ss92,fun	
		1.9036	Mg II, C IV	0.85-1.95	Mg II	ss92,fun	Y
0232–042	1.438	1.425	C IV	1.0-1.45	C IV	y91	Y
				0.1-1.45	Mg II		
0256–005	1.9951	~1.9951	C IV	1.58-2.05	C IV	fun	Y
				0.43-0.75	Mg II	fun	Y
0352+123	1.60	1.4831	Mg II	1.55-1.62	C IV	jhb91	
		1.5971	C IV	0.4-1.7	Mg II	btt90	Y
		1.6007	Mg II			btt90	Y
0736–063	1.901	1.2009	Mg II	1.25-1.95	C IV	abe94	
		1.2035	Mg II	0.25-1.91	Mg II	abe94	
		1.8175	C IV			abe94	
		1.9131	C IV			y91	Y
		1.9310	C IV			y91	Y
0808+289	1.887	0.6492	Mg II	1.65-1.9	C IV	y91	
		1.0472	Mg II	0.4-1.7	Mg II	y91	
		1.1417	Mg II			y91	
		1.8332	C IV			btt90	Y
		1.8753	C IV			btt90	Y
0831+101	1.76	1.7589	C IV	1.6-1.76	C IV	y91	Y
				0.4-1.7	Mg II	y91	
0835+580	1.534	1.4353	Mg II	1.25-1.55	C IV	jhb91	
		1.4383	Mg II	0.22-1.55	Mg II	btt90	
		1.5322	C IV			jhb91	Y
		1.5347	C IV			jhb91	Y
		1.5431 ^a	Mg II, C IV			jhb91,abf97	Y

Table 3—Continued

Name	z_{quasar}	z_{abs}	Ion	Redshift Search Interval	Ion	References	Ass. Abs.?
0926+117	1.75	none		1.70-1.75	C IV	btt90	
				0.4-1.75	Mg II	btt90	
0952+179	1.472	0.2378	Mg II	1.0-1.5	C IV	y91	
				0.11-1.5	Mg II		
1018+348	1.404	1.29	C IV	1.05-1.45	C IV	fun	
		~1.403	C IV	0.14-0.78	Mg II	fun	Y
		~1.406	C IV			fun	Y
1126+101	1.516	1.4389	C IV	1.1-1.5	C IV	y91	
		1.5098	C IV	0.14-0.52	Mg II	y91	Y
		1.5173	C IV			y91	Y
1218+339	1.52	0.7423	Mg II	1.03-1.55	C IV	abe94	
		1.5000	Mg II, C IV	0.12-1.55	Mg II	abe94	Y
1221+113	1.755	1.6144	Mg II	1.5-1.75	C IV	btt90	
				0.4-1.75	Mg II		
1258+404	1.66	none		1.55-1.65	C IV	btt90	
				0.4-1.65	Mg II	btt90	
1416+067	1.430	1.2734	C IV	1.2-1.6	C IV	y91	
		1.3751	C IV	0.14-0.53	Mg II	y91	
		1.4348	C IV			y91	Y
		1.4380	C IV			y91	Y
		1.4408	C IV			y91	Y
1556+335	1.646	1.2321	C IV	1.1-1.65	C IV	y91	
		1.6030	C IV	0.15-1.65	Mg II	jhb91	Y
		1.6106	C IV			jhb91	Y
		1.6129	C IV			jhb91	Y
		1.6395	C IV			jhb91	Y
		1.6445	C IV			jhb91	Y
		1.6505	Mg II, C IV			jhb91	Y
		1.6519	Mg II, C IV			jhb91	Y
		1.6537	Mg II, C IV			jhb91	Y
2044–168	1.939	1.3285	Mg II	1.45-1.95	C IV	y91	
		1.5586	C IV	0.35-0.75	Mg II	y91	
		1.7325	C IV	1.2-1.95	Mg II	y91	
		1.7341	C IV			y91	
		1.7355	C IV			y91	
		1.9199	C IV			y91	Y
		1.9213	C IV			y91	Y
2149+212	1.5359	0.9114	Mg II	1.5-1.55	C IV	y91	
		1.0073	Mg II	0.4-1.55	Mg II	y91	
2345+061	1.54	none		1.50-1.55	C IV	btt90	
				0.4-1.55	Mg II		

Note. — Only C IV or Mg II absorbers are listed, one absorber per line. Also listed is the redshift search interval, the redshift range which has been searched for C IV or Mg II absorption, as indicated. “Ass. Abs.?” refers to whether or not the particular absorber is an associated absorber.

^aAldcroft, Bechtold & Foltz (1997) report variability in this system (measured at $z=1.5425$, not 1.5431, in their spectra) over 3.9 years rest frame. This means this absorption system is very probably intrinsic to the quasar.

References. — abe94: Aldcroft, Bechtold & Elvis (1994); abf97: Aldcroft, Bechtold & Elvis (1994); bah93: Bahcall *et al.* (1993); btt90: Barthel, Tytler & Thomson (1990); bt96: Burles & Tytler (1996); fcw88: Foltz, Chaffee & Wolfe (1988); fun: Foltz *et al.*, unpublished; jhb91: Junkkarinen, Hewitt & Burbidge (1991), see also Junkkarinen, Hewitt & Burbidge (1992); ssh97: Sowinski, Schmidt & Hines (1997); ss92: Steidel & Sargent (1992); wil95: Wills *et al.* (1995); y91: York *et al.* (1991).

Table 4. Extinction, Magnitude Limits, and Seeing in Observed Fields

Field	Gal. Ext.	5σ K_s lim	K_s band 3σ lim	K_s band seeing	r band 3σ lim	r band seeing	Other filters 3σ lim, seeing	Area, arcmin ²
Q 0003–003 ^d	0.0132	20.0 ^a	20.823	1.51	25.285	1.67	...	6.894
Q 0017+154 ^d	0.0253	20.962	21.512	1.09	25.890	1.57	...	7.684
Q 0033+098	0.0472	21.006	21.556	1.51	25.363	1.39	...	5.480
Q 0149+218	0.0612	19.724 ^a	20.307	1.21	25.760	1.66	...	7.261
Q 0232–042	0.0053	19.5	21.470	1.25	25.540	1.72	...	7.598
Q 0256–005	0.0712	20.906	21.456	1.21	24.450	1.39	...	5.680
Q 0352+123	0.1892	19.0	20.344	1.45	24.985	1.51	...	6.413
Q 0736–063	0.27 ^b	...	21.205	1.12	24.177	1.39	...	5.493
Q 0808+289	0.0322	20.906 ^c	21.456	1.51	25.330	1.55	...	6.835
Q 0831+101	0.0333	21.513 ^c	22.063	1.24	25.501	1.18	...	6.815
Q 0835+580 ^d	0.0522	21.241	21.791	1.21	25.838	1.28	$H:20.896,1.27$ $J:23.689,1.37$ $z:24.990,1.64$ $i:24.928,1.18$	8.527
Q 0926+117	0.0153	20.689	21.239	1.45	25.447	1.12	...	5.568
Q 0952+179	0.0203	21.230	21.780	1.60	25.622	1.21	$J:23.807,1.39$	8.613
Q 1018+348	0.0000	20.359	20.909	1.48	25.705	1.27	...	7.605
Q 1126+101	0.0263	20.788	21.338	1.15	25.877	1.36	$H:20.939,1.12$ $J:23.226,1.46$ $z:25.009,1.87$	8.585
Q 1218+339 ^d	0.0002	20.677	21.227	1.42	25.529	1.21	...	7.936
Q 1221+113	0.0072	20.864	21.414	1.22	25.599	1.33	...	7.157
Q 1258+404 ^d	0.0000	21.613 ^c	22.163	1.45	25.818	1.15	$J:23.479,1.66$ $I:23.923,1.54$	9.199
Q 1328+254 ^d	0.0062	19.0	20.099	2.20	25.844	1.36	...	6.695
Q 1416+067 ^d	0.0072	20.691	21.241	1.30	25.812	1.45	...	7.071
Q 1430-0046	0.0233	19.229 ^a	19.785	1.66	25.224	1.51	...	7.028
Q 1437+624	0.0012	18.5 ^c	20.245	1.30	25.318	1.33	...	7.673
Q 1508–055	0.0542	1.91
Q 1556+335	0.0183	20.169 ^a	20.719	1.25	25.593	1.18	...	7.174
Q 1606+106	0.0432	20.0 ^c	20.753	1.43	25.420	2.23	...	5.543
Q 1718+481	0.0213	20.0	20.530	1.45	23.925	1.75	...	7.446
Q 1739+522	0.0333	19.0 ^c	20.704	1.27	25.776	1.24	...	6.258
Q 2044–168	0.0492	20.148 ^a	20.698	1.21	25.408	1.69	...	5.502
Q 2144+092	0.0542	18.0 ^c	21.138	1.78	25.098	1.69	...	7.593
Q 2149+212	0.0822	20.639	21.189	1.54	25.558	1.27	...	6.690
Q 2230+114	0.0422	20.168 ^a	20.749	1.63	25.327	1.66	...	7.316
Q 2325+293	0.0702	20.164	20.742	1.39	25.424	1.28	...	6.012
Q 2345+061	0.0653	21.169	21.719	1.58	25.111	1.42	$J:23.072,2.68$	9.347
CtrlFld1	0.0273	20.525	21.075	1.12	24.738	1.05	...	9.435
CtrlFld3	0.0192	20.726	21.276	1.60	24.743	1.05	...	9.343

^a $3\sigma_{sky}$ limit above sky used instead of $2.5\sigma_{sky}$ (see §3.6.3).

^bAssumed value.

^cMinimum detection area larger than 1.9 arcsec² used (see §3.6.3).

^d*HST* archival WFPC2 data of useful depth available (see §3.6.4).

Note. — Galactic extinction “Gal. Ext.” is $E(B-V)$. 5σ K_s limit magnitudes with only three significant digits are fields where, for various regions, detections are not reliable down to the nominal 5σ limits, but only to the values listed (see §3.6.3). Seeing measurements are in arcseconds. Area given is the overlapping area between r and K_s images, as well as J for all fields with J data except Q 2345+061.

Table 5. K_{UKIRT} Galaxy Counts: Our Control Fields

K	$\log N$	Poisson Uncertainties		RMS Uncertainties		Area (arcmin ²)	Number of Fields
		Lower	Upper	Lower	Upper		
15.25	2.585	0.448	0.367	2.585	0.384	18.778	2.0
15.75	2.888	0.296	0.354	0.003	0.003	18.778	2.0
16.25	3.190	0.210	0.248	0.544	0.234	18.778	2.0
16.75	3.067	0.339	0.296	3.067	0.382	18.778	2.0
17.25	3.704	0.119	0.125	0.610	0.244	18.778	2.0
17.75	3.494	0.150	0.162	0.003	0.003	18.778	2.0
18.25	3.592	0.150	0.162	0.003	0.003	18.778	2.0
18.75	3.854	0.105	0.111	0.333	0.186	18.778	2.0
19.25	4.227	0.069	0.072	0.169	0.121	18.778	2.0
19.75	4.245	0.069	0.073	0.019	0.018	18.559	2.0
20.25	4.348	0.067	0.070	0.065	0.057	16.718	2.0
20.75	4.614	0.063	0.066	0.302	0.176	12.219	2.0

Note. — Units of N are number mag⁻¹ deg⁻². Number of fields refers to the two separate control field pointings used to calculate the RMS errors.

Table 6. K_{UKIRT} Galaxy Counts: Literature Average

K	$\log N$	Poisson Uncertainties		RMS Uncertainties		Area (arcmin ²)	Number of Surveys
		Lower	Upper	Lower	Upper		
12.75	1.379	0.451	0.366	0.108	0.086	600.808	3.0
13.25	0.816	0.739	0.558	0.816	0.446	781.608	4.0
13.75	1.519	0.162	0.214	0.516	0.229	1668.088	7.0
14.25	1.708	0.144	0.168	0.304	0.177	1668.088	7.0
14.75	2.136	0.103	0.101	0.159	0.116	1668.088	7.0
15.25	2.462	0.071	0.061	0.108	0.086	1668.088	7.0
15.75	2.772	0.039	0.038	0.118	0.093	1684.598	8.0
16.25	3.001	0.051	0.029	0.102	0.082	1684.598	8.0
16.75	3.279	0.058	0.025	0.075	0.064	1196.398	9.0
17.25	3.534	0.027	0.026	0.183	0.128	565.878	8.0
17.75	3.699	0.031	0.022	0.147	0.109	565.878	8.0
18.25	3.889	0.019	0.019	0.179	0.126	511.638	9.0
18.75	4.077	0.027	0.027	0.125	0.097	294.928	9.0
19.25	4.231	0.041	0.037	0.104	0.084	278.998	8.0
19.75	4.341	0.051	0.056	0.104	0.084	59.499	6.0
20.25	4.442	0.046	0.046	0.156	0.115	33.898	7.0
20.75	4.639	0.040	0.044	0.164	0.119	27.609	7.0
21.25	4.782	0.049	0.054	0.172	0.123	13.590	5.0
21.75	4.913	0.048	0.057	0.127	0.098	7.380	3.0
22.25	5.032	0.041	0.052	0.147	0.110	5.370	3.0
22.75	5.172	0.052	0.057	0.131	0.101	4.210	2.0
23.25	5.367	0.057	0.060	0.096	0.079	4.210	2.0
23.75	5.597	0.085	0.085	0.095	0.078	2.880	1.0

Note. — Units of N are number mag⁻¹ deg⁻². Number of surveys refers to the number of separate surveys used to calculate the RMS errors.

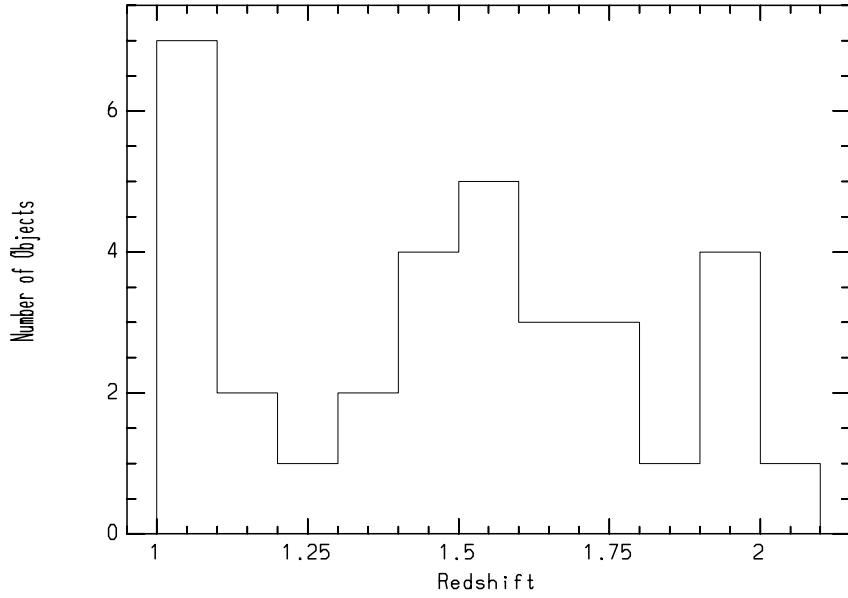


Fig. 1.— Redshift histogram of all $z > 1$ quasars observed.

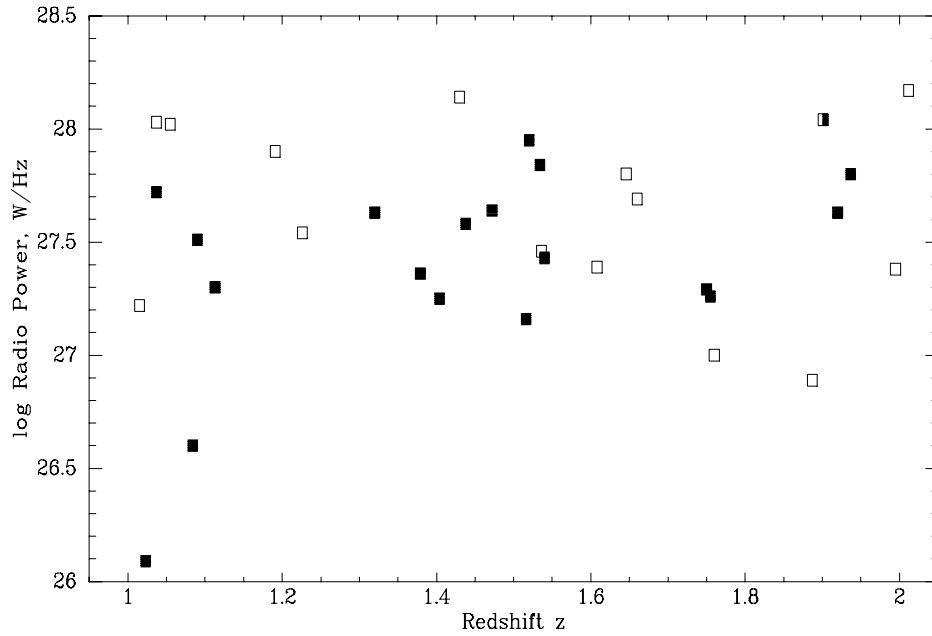


Fig. 2.— Radio Power $\log(P)$ at 5 GHz rest frequency plotted vs. redshift for the $z > 1$ quasars. Filled symbols are steep-spectrum objects, open symbols are flat-spectrum objects, and the half-filled symbol has unknown radio spectral slope.

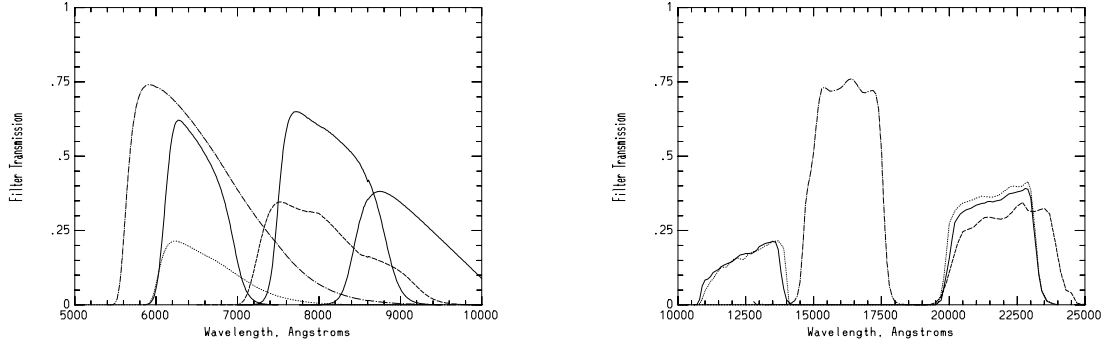


Fig. 3.— a. Transmission of all optical filters used, including detector QE. Primary filters are Gunn r , i , and z with Steward 800x1200 CCD (solid); other filters used are Kron-Cousins R_C with Steward 800x1200 CCD (dash-dot), Kron-Cousins I_C with Steward 2kx2k CCD (dashed), and “Osmer/Green” R' with old KPNO Tek2048 (dotted). For clarity, Gunn riz with the lower-QE Steward 2kx2k CCD are not shown, although some observations were made with those filter-instrument combinations. b. Transmission of all IR filters used, including detector QE: KPNO J and IRTF H with NSFCAM (dot-dash), and Steward K with Steward 256x256 (dashed). NSFCAM is an InSb array while IRIM and the Steward 256x256 are HgCdTe, which accounts for the different throughput in J and K_s compared to H . Note the wavelength scale is three times larger than in a.

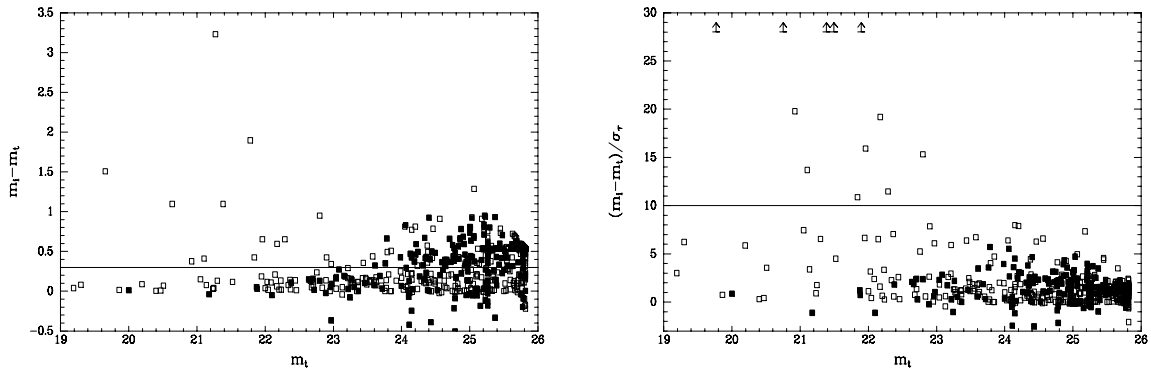


Fig. 4.— a) Aperture correction $m_i - m_t$ between total and isophotal FOCAS magnitudes plotted against FOCAS total magnitude m_t for all objects in the r image of the Q 0835+580 field. b) Uncertainty-normalized aperture correction $(m_i - m_t) / \sigma_t$ plotted against m_t . Lower limits indicate objects with values off the graph. Objects never split by FOCAS are shown as filled boxes, and open boxes are objects split by FOCAS. Objects above the lines in both diagrams are considered to have erroneous m_t , as are objects with $m_i - m_t < 0$.

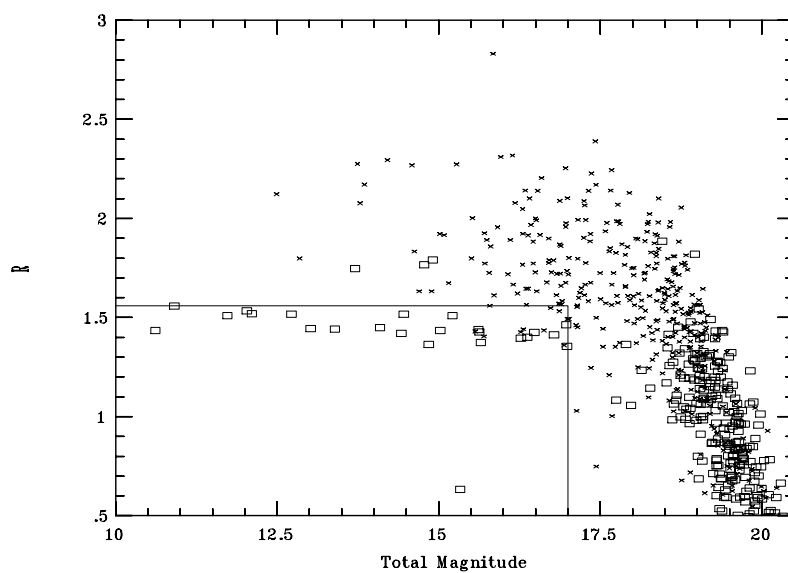


Fig. 5.— Resolution parameter $R=m_c-m_t$ is plotted against FOCAS total magnitude m_t for all objects in the summed image of the Q 0835+580 field. Objects classified as stars by FOCAS are shown as boxes and all other objects as crosses. Objects below and to the left of the lines are classified as stellar.

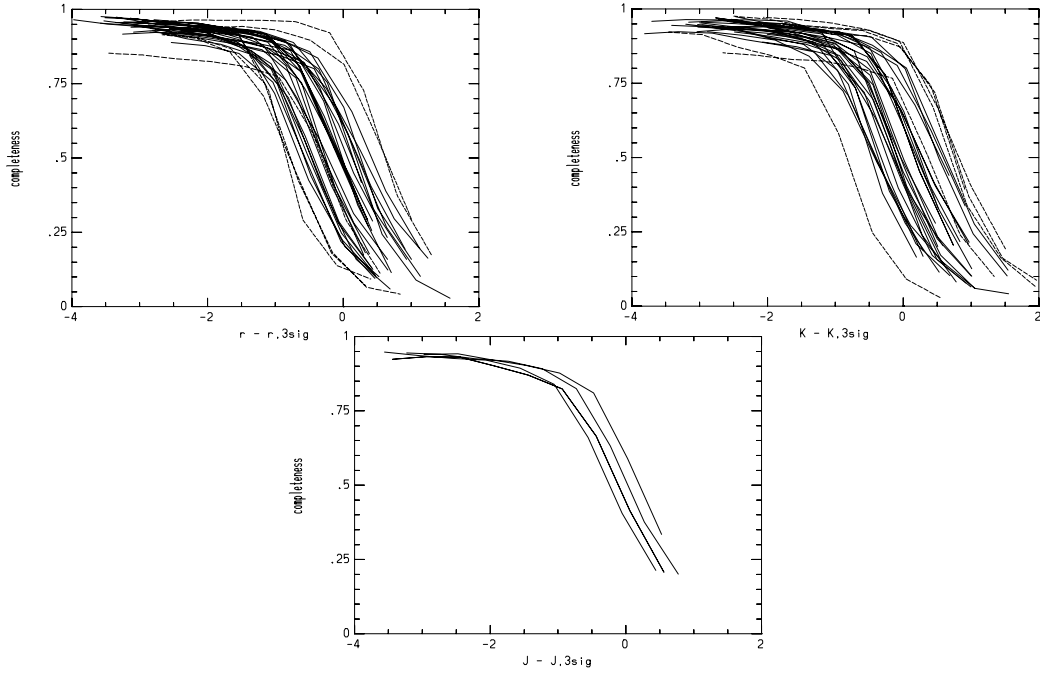


Fig. 6.— Completeness vs. magnitude relative to 3σ limiting magnitude. a) r -band completeness. b) K_s -band completeness. c) J -band completeness for the four fields where detection was done on $r + J + K_s$ images. Dashed lines indicate fields not used in calculating number-magnitude counts. All three filters (rJK_s) show the expected decline from $>90\%$ completeness at bright magnitudes to $\sim 50\%$ at the 3σ limiting magnitude and $<20\%$ one magnitude fainter than the 3σ limit.

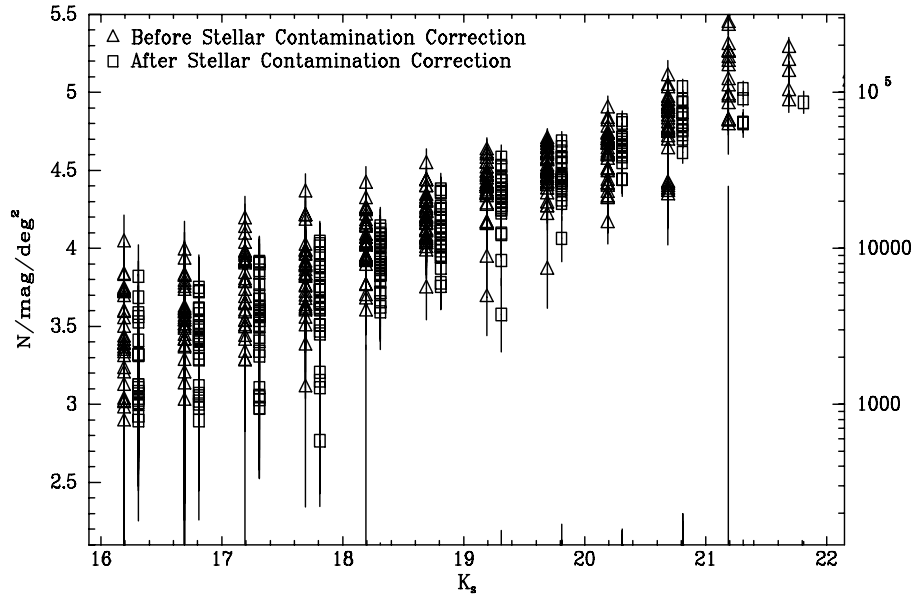


Fig. 7.— The K_s $N(m)$ relation for all 31 good fields with $|b| > 20^\circ$ is shown before (triangles) and after (squares) stellar contamination correction, offset for clarity. 1σ Poisson errors are shown for all points. Post-correction fields are only plotted down to the 50% completeness magnitude.

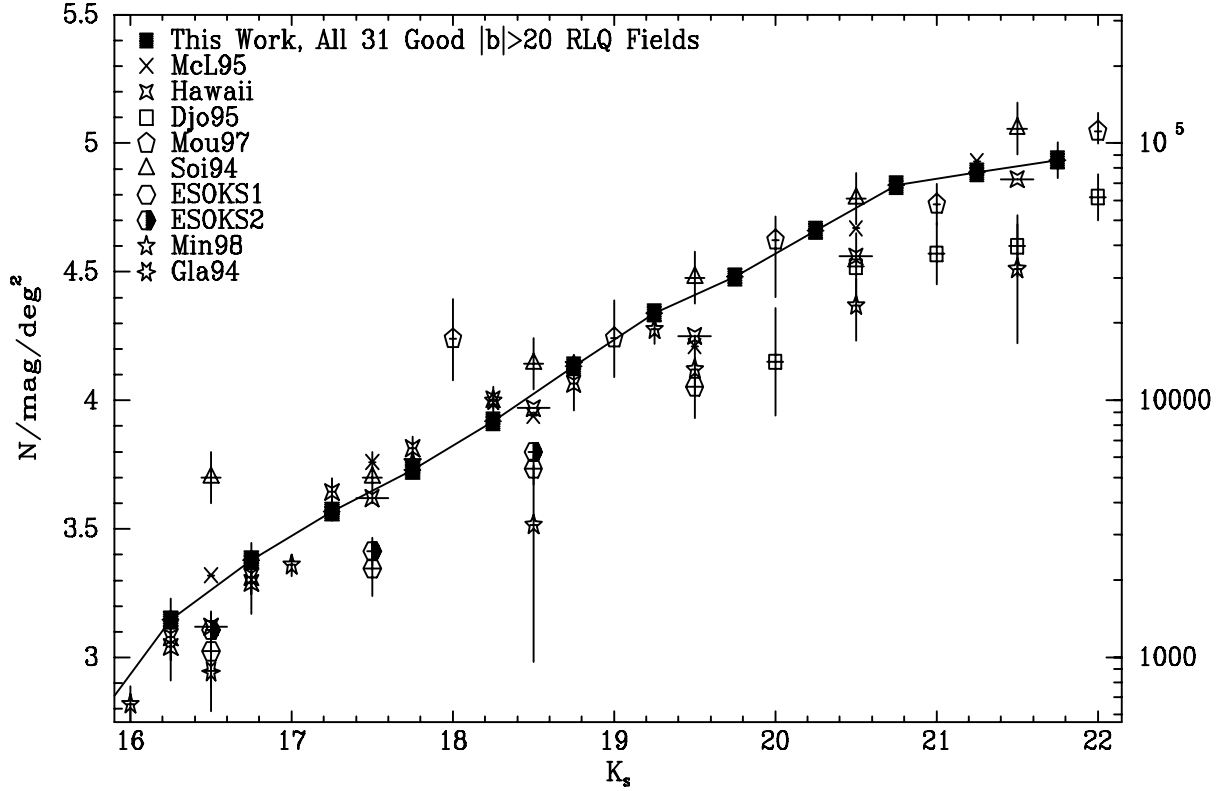


Fig. 8.— The average K_s $N(m)$ relation for all 31 good RLQ fields with $|b| > 20^\circ$ is shown as the solid squares connected by the solid line. 1σ Poisson errors on $N(m)$ are shown for all our points but are often smaller than the symbols. Also shown are 1σ RMS uncertainties on the zeropoints of the magnitude scales of the different surveys, as given by the authors. (These do not include systematic uncertainties; see §4.1.) These error bars are also often smaller than the symbols. Our bins are separated by $0^m.5$ magnitudes but have been normalized to number of galaxies per magnitude bin, as well as per square degree. $N(m)$ data and 1σ Poisson errors from the literature are plotted as various symbols. Uncertainties for the Soifer *et al.* (1994) points are estimates. Reference codes are as follows: McL95: McLeod *et al.* (1995); Hawaii: Hawaii Medium Deep, Medium Wide, and Deep Surveys: Gardner, Cowie & Wainscoat (1993), Gardner (1995ab), and Cowie *et al.* (1994); Gla94: Glazebrook *et al.* (1994); Djo95: Djorgovski *et al.* (1995); Mou97: Moustakas *et al.* (1997); Soi94: Soifer *et al.* (1994); ESOKS1 & ESOKS2: Saracco *et al.* (1997); Min98: Minezaki *et al.* (1998a).

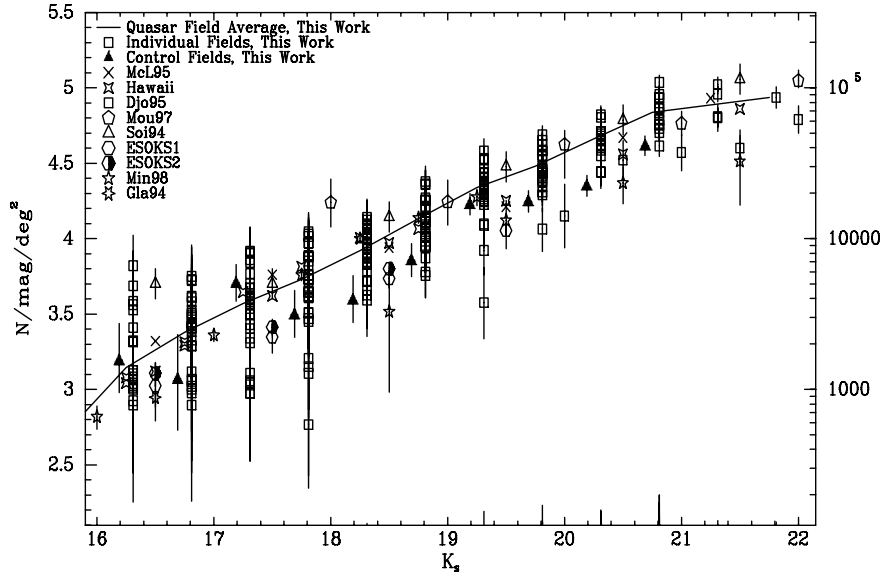


Fig. 9.— The average K_s $N(m)$ relation for all 31 good fields with $|b| > 20^\circ$ is shown as the solid line. Individual fields are shown down to their 50% completeness magnitudes as open squares and 1σ Poisson errors (offset $+0^m.06$ for clarity). Our control fields (offset $-0^m.06$ for clarity) are shown as filled triangles. Literature points are the same as in Figure 8.

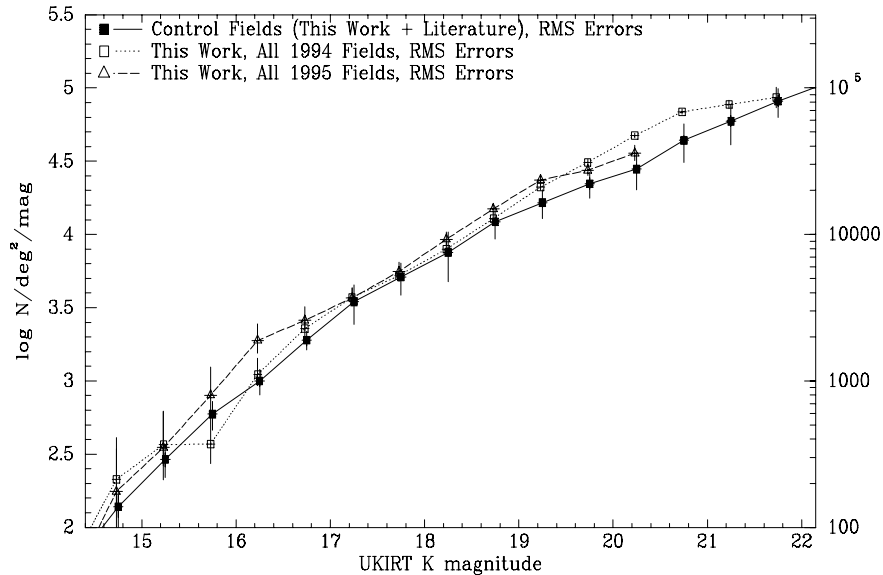


Fig. 10.— The K_{UKIRT} $N(m)$ relations for our 1994 and 1995 KPNO 4m data are plotted as dotted and dashed lines respectively. The area-weighted average of our control fields and all published random-field imaging surveys (corrected to K_{UKIRT}) is plotted as the solid line, along with RMS errors on the $N(m)$ values and formal uncertainties on the magnitude bin centers (see text).

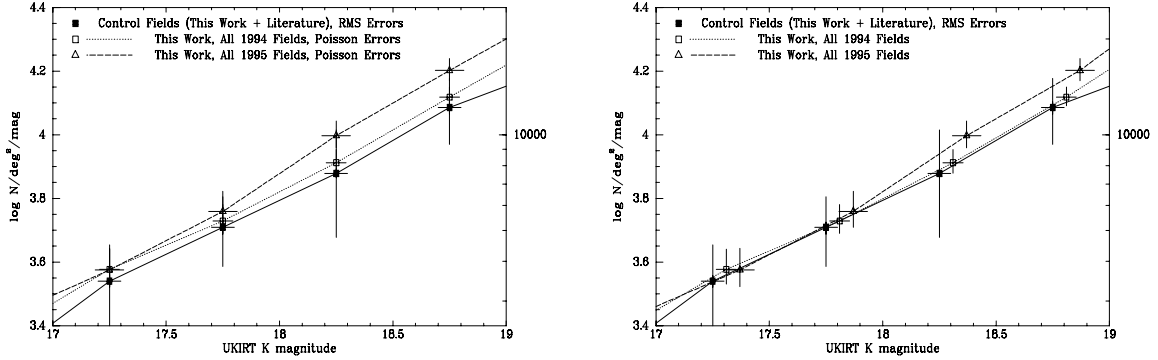


Fig. 11.— The K_{UKIRT} $N(m)$ relations for our 1994 and 1995 KPNO 4m run data are plotted as dotted and dashed lines respectively. The area-weighted average of our control fields and all published random-field imaging surveys (corrected to K_{UKIRT}) is plotted as the solid line. RMS errors are plotted for the control field $N(m)$ values, and Poisson errors for the quasar fields. Formal uncertainties are plotted for the magnitude bin centers (see text). a. The $N(m)$ relation after correction to the UKIRT magnitude scale. b. The $N(m)$ relation after further correction for systematics in our data.

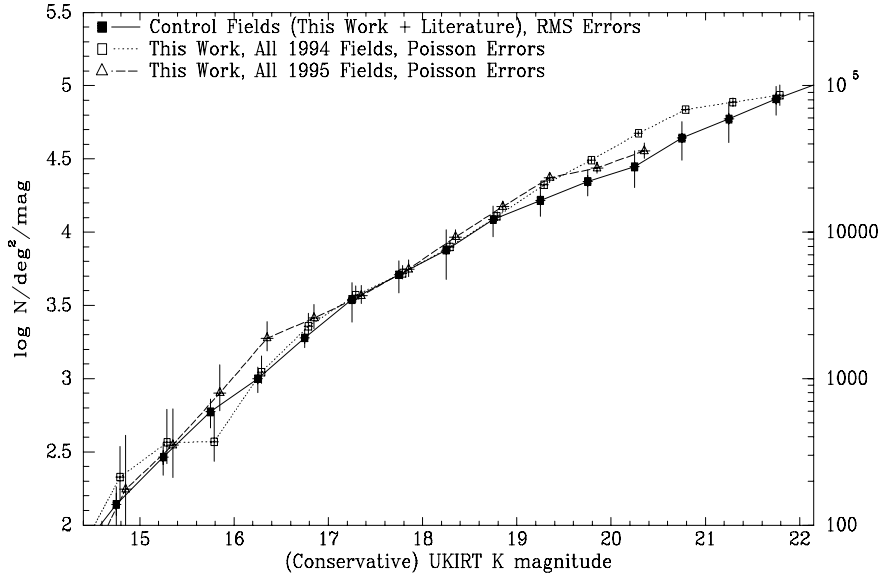


Fig. 12.— The conservative K_{UKIRT} $N(m)$ relations for our 1994 and 1995 KPNO 4m run data are plotted as dotted and dashed lines respectively. The area-weighted average of our conservative-magnitude control fields and all published random-field imaging surveys (corrected to K_{UKIRT}) is plotted as the solid line. RMS errors are plotted for the $N(m)$ values and formal uncertainties for the magnitude bin centers (see text).